INVESTIGATION, MODELING, AND APPLICATIONS FEASIBILITY OF THE THERMAL CROSSTALK IN HIGH T_C TRANSITION EDGE BOLOMETER ARRAYS

A DISSERTATION SUBMITTED TO
THE DEPARTMENT OF ELECTRICAL AND ELECTRONICS
ENGINEERING
AND THE INSTITUTE OF ENGINEERING AND SCIENCE
OF BILKENT UNIVERSITY
IN PARTIAL FULFILLMENT OF THE REQUIREMENTS
FOR THE DEGREE OF
DOCTOR OF PHILOSOPHY

By
Ali Bozbey
August 2006

I certify that I have read this thesis and that in my opinion it is fully adequate, in scope and in quality, as a dissertation for the degree of doctor of philosophy.

Asst. Prof. Dr. Mehdi Fardmanesh(Supervisor)

I certify that I have read this thesis and that in my opinion it is fully adequate, in scope and in quality, as a dissertation for the degree of doctor of philosophy.

Asst. Prof. Dr. Özgür Aktaş

I certify that I have read this thesis and that in my opinion it is fully adequate, in scope and in quality, as a dissertation for the degree of doctor of philosophy.

Dr. Tarık Reyhan

I certify that I have read this thesis and that in my opinion it is fully adequate, in scope and in quality, as a dissertation for the degree of doctor of philosophy.

Assoc. Prof. Dr. Oğuz Gülseren

I certify that I have read this thesis and that in my opinion it is fully adequate, in scope and in quality, as a dissertation for the degree of doctor of philosophy.

Prof. Dr. Recai Ellialtıoğlu

Approved for the Institute of Engineering and Science:

Prof. Dr. Mehmet Baray
Director of the Institute

ABSTRACT

INVESTIGATION, MODELING, AND APPLICATIONS FEASIBILITY OF THE THERMAL CROSSTALK IN HIGH T_C TRANSITION EDGE BOLOMETER ARRAYS

Ali Bozbey
PhD in Electrical and Electronics Engineering
Supervisor: Asst. Prof. Dr. Mehdi Fardmanesh
August 2006

So far, the high T_c transition edge bolometer (TEB) devices are mostly used as single pixel detectors. Recently, there are a number of groups working on the 2-4 pixel array applications of the high T_c TEB. Though the target spectrum of the TEB is far IR and mm-waves, we are using a near IR laser source in our investigation due to practical reasons since the response analysis is similar.

We have designed and implemented 4-pixel $YBa_2Cu_3O_{7-\delta}$ (YBCO) edge transition bolometer arrays. The crosstalk study was made possible through the illumination of the sense-devices and measuring the voltage response of the blocked read-out device in the same array. This was done using a silver coated shadow mask. In order to prevent thermal artifacts created by the mask, the mask was made in free standing configuration on top of the devices. The devices were made of 200 nm and 400 nm thick pulsed laser deposited YBCO films on $SrTiO_3$ and $LaAl_2O_3$ substrate materials.

In this thesis, we made the qualitative investigation of the dependence of the thermal crosstalk on the various device parameters such as the substrate material, device layout, YBCO film thickness, operating temperature, and modulation frequency. Then, based on the experimental results, we proposed an analytical thermal model. We proposed two models: i) Basic model, which takes into account only the lateral heat diffusion in the substrate for quick design purposes ii)Analytical model, which takes into account the lateral heat diffusion, vertical heat diffusion, and the effect of the leaking laser radiation through the shadow mask, for detailed design purposes and verifying the qualitative analysis. Finally, we proposed and verified possible applications of the thermal crosstalk in TEB arrays. One proposed application of the crosstalk is the electrical free read-out

of the sense pixels by utilization of the unique dependence of the magnitude and phase of the response on the thermal crosstalk between bolometer pixels in an array.

The qualitative investigation made in this study is the most detailed investigation about the bolometer arrays and the proposed analytical model is the strongest among the reported ones so far in terms of fitting the experimental results, explaining the effects of the various parameters, and designing TEB arrays. The proposed crosstalk based read-out method is expected to decrease the read-out circuitry for possible TEB based applications. Since multilayer process is difficult to make in high T_c superconductors, decreasing the complexity of the read-out circuitry by half is even important and it is the first time that such a method is utilized including bolometer arrays made of different types of materials.

Keywords: Superconductor, bolometer, infrared detector, thermal crosstalk, YBCO.

ÖZET

YÜKSEK SICAKLIK SÜPERİLETKEN BOLOMETRE DİZİLERİNDE TERMAL BAĞLAŞIMIN İNCELENMESİ, MODELLENMESİ VE UYGULAMA OLANAKLARI

Ali Bozbey
Elektrik ve Elektronik Mühendisliği, Doktora
Tez Yöneticisi: Yrd. Doç. Mehdi Fardmanesh
Auğustos 2006

Şimdiye kadar yüksek sıcaklık süperiletken geçiş kenarı bolometreleri (GKB) tek piksellik algılayıcılar olarak kullanılmışdır. Son zamanlarda bazı gruplar 2-4 piksellik yüksek sıcaklık GKB dizileri üzerinde çalışmaktadır. GKB'lerin asıl uygulama spektrumu uzak kızıl ötesi ve mm dalgaboyları olmasına rağmen, tepki analizi aynı olduğu için ölçümlerimizde pratik nedenlerden dolayı yakın kızılötesi lazer kaynağı kullanılmıştır.

Bu çalışmada 4×1 piksellik $YBa_2Cu_3O_{7-\delta}$ geçiş kenarı bolometre dizileri tasarlanıp üretildi. Komşu aygıtlar arasındaki termal bağlaşımın incelenmesi, aygıtlardan sadece birisinin lazer ile aydınlatılıp, maskelenmiş diğer aygıtların tepkilerinin ölçülmesiyle başarıldı. Maske olarak 400 nm gümüş kaplı 0.1 mm kalınlığında cam kullanıldı. Maske tarafından kaynaklanabilecek termal etkilerin engellenebilmesi için, maske, aygıtlara değmeden, aygıtların üzerinde serbest duracak şekilde üretildi. Aygıtlar için darbeli lazer kaplama yöntemiyle 200 nm ve 400 nm kalınlıklarında, $SrTiO_3$ ve $LaAl_2O_3$ alttaş üzerine yapılmış filmler kullanıldı.

Bu tezde, termal bağlaşımın, alttaş maddesi, aygıt tasarımı, YBCO film kalınlığı, çalışma sıcaklığı ve modulasyon frekansı gibi aygıt parametrelerine olan bağımlılığı incelendi. Daha sonra, deney sonuçlarına dayanarak, 2 adet termal model önerildi. Bunlardan birincisi, sadece substrat üzerinde yatay ısı dağılımını dikkate alan, hızlı tasarım maksatlı kullanılabilecek basit model, ikincisi ise, yatay ve dikey ısı yayılımını ve gümüş maskenin lazeri mükemmel engelleyememesini hesaba katan; daha ayrıntılı tasarım amaçlı ve bağlaşımın daha ayrıntılı incelenmesine olanak veren analitik modeldir. Son olarak, termal bağlaşımın olası

uygulama alanları önerildi ve bunların yapılabilirliği gösterildi. Olası uygulama alanı olarak, bağlaşım tepkisinin fazını ve büyüklüğünü kullanarak, elektriksel bağlantı yapmadan dizideki birden fazla pikselin tepkilerinin okunmasıdır.

Yapılan nitel inceleme bolometre dizileri ile ilgili şimdiye kadar yapılmış en ayrıntılı incelemedir. Önerilen termal model, şimdiye kadar rapor edilenler içinde, deney sonuçlarına uyması, çeşitli aygıt parametrelerinin etkilerini açıklaması ve GKB dizileri tasarlamada kullanılabilmesi açısından en güçlü modeldir. Önerilen tepki okuma yönteminin ise yüksek sıcaklık süperiletkenlerinde çok katmanlı tasarımlar yapmanın zorluğu dikkate alındığında, bolometre dizilerinin tepki okuma elektroniklerinin karmaşıklığını azaltmasının önemi anlaşılmaktadır. Bu yöntem bolometre dizilerinde ilk defa kullanılmıştır.

Anahtar sözcükler: Süperiletken, bolometre, kızıl ötesi detektör, termal bağlaşım, YBCO.

Acknowledgement

I would like to express my sincere gratitude to Dr. Mehdi Fardmanesh for his supervision, suggestions, and encouragement during my graduate studies.

I would also to thank Dr. Özgür Aktaş, Dr. Recai Ellialtıoğlu, Dr. Oğuz Gülseren, and Dr. Tarık Reyhan for reading the manuscript and commenting on the thesis.

I am indebted to Dr. J. Schubert for supplying YBCO films.

I would like to express my special thanks and gratitude to my fellow Rizwan Akram for sharing his experiences with me.

I would like to express my special thanks to İlbeyi Avcı for sharing the laboratory nights with me from msn.

Finally, I would like to give my special thanks to my wife Ismahan, my parents, and my sister Ayfer whose understandings made this study possible.

To Ismahan

Contents

List of Figures

List of Tables

Chapter 1

Introduction and Literature Survey

High temperature superconductor transition edge bolometers (TEB) are one of the promising devices that can be used to detect electromagnetic radiation over the whole spectrum from X ray to the far infrared. They cover a wide range of applications such as space radiometry and spectrometry, optical communication, thermal sensing, and imaging for military or biomedical purposes. The operation of a bolometer is basically based upon the steep drop in the resistance at the superconductivity transition. Over the last decade, especially after the discovery of high T_c superconductor $YBa_2Cu_3O_{7-\delta}$ (YBCO), there has been quite a considerable research on single pixel bolometer detectors [1]– [9]. In the recent years, the array applications of the transition edge bolometers have attracted attention and a number of groups are working on the fabrication, modeling, and applications of TEB arrays [10] – [22].

In this thesis, we investigated the interpixel thermal crosstalk in an array of high T_c superconducting transition edge bolometers. We designed and fabricated various TEB arrays and analyzed the dependence of the interpixel thermal crosstalk on the physical parameters of the devices such as the YBCO film thickness, substrate material, and temperature. Besides, we derived an analytical

thermal model and proposed an example application of utilization of the thermal crosstalk. The results of more than ten experiments are used for qualitative explanation of the effects of the physical parameters and verification of the proposed analytical thermal model.

The thesis is organized as the following: In this chapter, we provide some background information about bolometers and thermal crosstalk that will help the reader to understand the crosstalk phenomena in the bolometer arrays. In the second chapter, we explain the fabrication details of the devices and show the main parts of the experimental setup together with the measurement methodology. In the third and fourth chapters, which are based on articles [23] – [25], we show the experimental results and propose a thermal model to explain the experimental results respectively. Then in the fifth chapter, which is based on article [26], we propose a possible application of the thermal crosstalk in the bolometer arrays.

Throughout this thesis, the "bolometer" and "device" terms will be used to represent "superconducting transition edge bolometer", and "crosstalk" will represent "interpixel thermal crosstalk" in the bolometer arrays.

The principles of the operation of a single pixel bolometer has been explained in the MS theses of the author and Akram in details [27], [28]. Hence, in this thesis only a condensed summary will be provided and the focus will be mainly on the arrays and the crosstalk phenomena in these devices.

1.1 Operation of a Transition Edge Bolometer

Bolometer is a detector whose electrical resistance changes (+ or -) with temperature. Temperature change is caused by the absorbed radiation or by heat diffusion in the substrate (crosstalk) as shown in Figure 1.1. Theoretically bolometers can be made by using any conductor the resistance of which has temperature dependence. However, for sensitivity, the temperature dependence of the resistance (dR/dT) should be as high as possible. Superconductors are perfect candidates for this purpose since there is a sharp resistance drop at the normal to superconductor transition. Thus, at the edge of the normal to superconductor transition, there is a considerable resistance change due to a small amount of temperature rise. The operation of a superconducting transition edge bolometer (TEB) is explained in Figure 1.2.

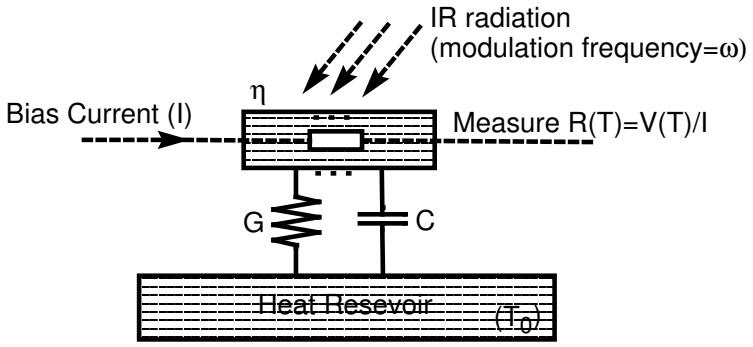

Figure 1.1: Schematic of a bolometer with thermal conductance G and capacitance C.

For maximum sensitivity, the temperature of the bolometer should be kept constant at the edge of the transition. For $YBa_2Cu_3O_{7-\delta}$ material which we used in this thesis, the transition temperature is around 90 K and the transition width is around 1 K. For the operation of this bolometer, it is enough to control the temperature at the T_c with 20 mK accuracy, which is achievable with a PID controller. However, if the bolometer material is Tungsten, (W), which has a critical temperature of 125 mK and transition width of just 1 mK, there is no way to externally control the temperature of the device with the present

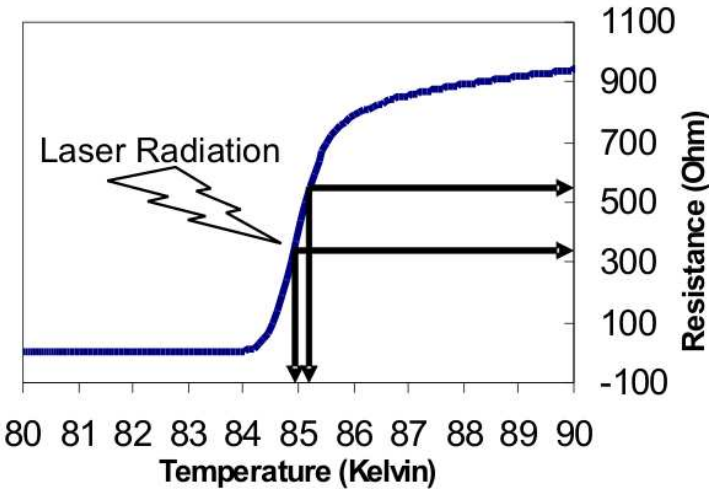

Figure 1.2: Operation of a bolometer: Incident radiation is absorbed by the superconducting film and its temperature is increased which causes an increase of resistance.

technique. Thus, the bias voltage is used to achieve both electrical bias and temperature bias. Applying a voltage across the W film causes it to self-bias in the resistive transition due to Joule heating, and its temperature can be determined by measuring the electrical current flow through the metal (negative feedback). W material is used for single photon detector applications as explained in Section 1.2.2.

Detection of the radiation (resistance change) by edge transition bolometers can be done in two methods. In the conventional method, a constant bias current is applied to the bolometer and the change of resistance is measured by means of the voltage change around the device. However, in the SQUID based read-out method, the bolometer is biased with a constant voltage and the change in the resistance is sensed by a SQUID that senses the resulting change in the current through the device [29]. Utilizing the SQUID, which is the most sensitive magnetic field or current sensor, is superior to the conventional method.

In this thesis we utilized the conventional method since our goal was investigation of the response rather than increase of sensitivity. For the targeted

measurements, the conventional method was sufficient. The details of the experimental setup is explained in Chapter 2. For the details of SQUID based read-out of transition edge bolometers, the reader can refer to articles [12], [13], [30] – [32].

1.2 Application Areas

1.2.1 Astronomy - mm-wave and THz Detectors

The millimetre region of the electromagnetic spectrum can be defined as 10 mm> λ >1 mm (30 GHz< ν <300 GHz) and the sub-millimetre (THz) as 1 mm> λ >0.2 mm (300 GHz< ν <1500 GHz). The universe emits as much energy in the mm and sub-mm region as the optical, near IR and UV. Many astrophysical phenomena can be studied in the mm and sub-mm, which cannot be studied using the emission in the optical and IR region. For example by using the Sunyaev-Zel'dovich Effect (scattering of the cosmic microwave background) as it passes through clusters of galaxies, the expansion history of the universe, the formation of the structure can be explained [33], [34]. There are a number of groups working in the Astrophysical applications of the transition edge bolometers [33] – [39].

As Biswas states, [35], "Bolometer devices are all set to dominate mm and sub-mm wave astronomical instrumentation in the coming decades due to their quick detector response, high sensitivity, and wide bandwidth of operation." Currently, in a number of space telescopes TEB sensors are being used. For example, in the Atacama Pathfinder EXperiment (APEX), which is a collaboration between Max Planck Institut fur Radioastronomie (MPIfR) , Onsala Space Observatory (OSO), and the European Southern Observatory (ESO), an array of 288 composite bolometers with superconducting thermistors and superconducting quantum-interference devices (SQUIDs) for multiplexing and amplification is in preparation. The goal of the experiment is to study warm and cold dust in star-forming regions both in Milky Way and in distant galaxies [40]. In 2001, Romani *et al.* reported observations of the Crab pulsar made during prototype testing at the McDonald 2.7 m with a fiber-coupled transition-edge sensor (TES) system. The detector system used in the observations had a 6×6 array of Tungsten TES pixels on a Si substrate [39].

1.2.2 Single Photon detection

To measure the energy associated with a single particle, an extremely sensitive detector is required. For example, single photon detection is important for ultimate security of a quantum cryptography or quantum key distribution systems. If the source departs from ideal operation by emitting more than one photon in the same quantum-bit state, single photon sources can be destroyed by a host of attacks. So, the researchers have developed true single photon sources [41]. However, the security of quantum cryptography systems can also be compromised if the detectors used in the receiving system have high error rates. Thus, very low noise single photon detectors are required as well [42] – [44].

Miller *et al.* report a system based on the superconducting transition edge bolometer that is originally developed for astronomical spectrophotometers [39]. As explained in Section 1.1, the TEB device produces an electrical signal proportional to the heat produced by the absorption of a photon. The increase in temperature of the absorber is measured by an ultrasensitive thermometer (=bolometer) consisting of a tungsten film with a very narrow superconducting-to-normal resistive transition (T_c=125 mK, ΔT_c=1 mK). The detection efficiency of the system is 20% and the NEP for the system is below $1 \times 10^{-19}\ W/Hz^{1/2}$ [42], [45].

1.2.3 X-Ray Detectors

X-ray spectrometers are used in X-ray microanalysis and X-ray astronomy. Semiconductor energy-dispersive spectrometer (EDS) is used in over 90% of installed X-ray microanalysis systems because it is easy to use, inexpensive to operate, and offers rapid qualitative evaluation of chemical composition. However, it is limited by an energy resolution on the order of 100 eV, which is insufficient to resolve many important overlapping X-ray peaks in materials of industrial interest. On the other hand, semiconductor wavelength-dispersive spectrometer (WDS) uses Bragg reflection from curved difracting crystals to achieve high resolution (typically 2 to 20 eV) needed to resolve most peak overlaps. However, qualitative

WDS analysis is limited by the long time needed to serially scan over the entire energy range using multiple difraction crystals [46].

Finkbeiner *et al.*, Wollman *et al.*, and Irwin *et al.* report superconducting bilayer transition edge bolometers for X-ray Microcallorimetry [46]–[48]. Basically, their microcalorimeters consists of an X-ray absorber and a transition edge bolometer underneath. When an X-ray deposits its energy in the absorber, the temperature and resistance of the TES increase. As explained in Section 1.1, the increase of the resistance can be sensed with a SQUID sensor or lock-in amplifier. For example, Wollman *et al.* has used Bi as the absorbing layer and Al/Ag as the transition edge bolometer. The bolometer has an operating temperature of around 100 mK and 2eV energy resolution.

1.2.4 Medical Imaging

Starting with the invention of the X-rays, by Wilhelm Conrad Röntgen in 1895, X-ray examination has become an invaluable tool in medical diagnosis. However, this technique has several shortcomings. X-rays are harmful to living beings since they are ionizing. In addition, the spatial resolution is limited by Rayleigh scattering to about 50 μm. Finally, the contrast between some sorts of tissues is quite low [49], [50]. Methods have recently been developed that make use of terahertz (THz) frequencies, the region of the spectrum between millimetre wavelengths and far infrared, for imaging purposes. Radiation at these wavelengths is non-ionizing and subject to far less Rayleigh scatter than visible or infrared wavelengths, making it suitable for medical applications [51].

In 1995, Hu *et al.* took the first image in the frequency range of 0.1 to 2 THz [52]. Later they have developed their system up to the point where two-dimensional images of objects a few centimeters in size could be accumulated in a reasonable time. In 1998, Hunsche *et al.* has increased the spatial resolution by near-field imaging, and resolutions down to $\lambda/6$ have been reported. They have shown that the internal structure and composition of objects can be visualized using THz tomography [53]. Later, Han *et al.* and Arnone *et al.* could identify

different types of tissues in fresh untreated samples [54], [55]. Mittleman and co-workers showed that THz imaging may be useful for burn diagnosis [56], [57]. In 1999 and 2001, skin cancer detection has been demonstrated by Arnone and co-workers [55], [58].

In the year 2000, the first commercially available THz time-domain imaging system has been developed by Rudd *et al.* [59]. However, still there is a need for smaller and less expensive systems.

Knobloch *et al.* report on a THz imaging investigation of samples that are treated by the standard procedure for histo-pathological examination. In [49], they present data obtained on a pig larynx and a human liver with metastasis. Their measurements show that different types of tissue can be clearly distinguished in THz transmission images, either within a single image or by comparing images obtained for different frequency windows. For the measurements they presented, the frequency spacing is set to 230 GHz which is the resonance frequency of their low-temperature-grown GaAs dipole antenna. For detection, a low T_c standard bolometer is used. They aim on detection schemes which use nitrogen cooled high-temperature superconductor bolometer.

In the year 2003, a superconducting nanotransistor based digital logic gate has been reported [60], [61]. Though it is not a bolometric sensor application, it is worth mentioning here since the operation principle is based on the joule heating resulting in a temperature rise and diffusion of the heat in the device.

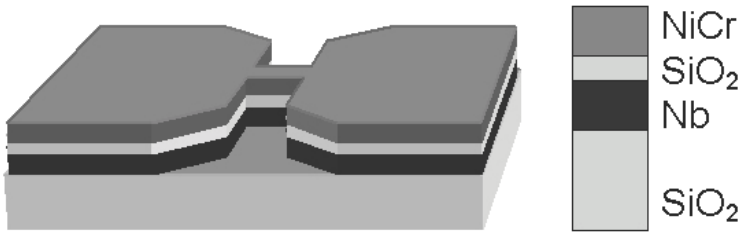

Figure 1.3: A schematic diagram of the nanotransistor [60].

The device consists of three component layers, the heater layer, the insulator layer, and the superconductor layer. When sufficient potential drop is applied to the heater, the electron temperature is raised significantly above the background temperature. This leads to the creation of nonequilibrium or hot phonons in the heater, which travel to the substrate. When the hot phonons arriving at the superconductor have energies less than the local superconducting energy gap (Δ) they will reach through the superconductor without scattering with the Cooper pairs and travel to the interface between the superconductor and the substrate, which acts as the phonon sink. When the phonon energy is higher than the minimum excitation energy, it will act to break the Cooper pairs exciting quasiparticles. The consequence of the increased population of excited quasiparticles is that it creates a situation equivalent to a local increase in temperature which will lead to the reduction in the superconducting order parameter. Then, this will reduce the local critical current. Basically, the heat generated by the top heater layer acts to control the flow of supercurrent through the weak-link giving transistor action in the device [60], [61].

1.3 Commonly used Substrates for $YBa_2Cu_3O_{7-\delta}$ thin film

Popular substrates used with YBCO are Lanthanum Aluminate ($LaAlO_3$), Magnesium Oxide (MgO), Neodymium Gallate ($NdGaO_3$), Saphire (Al_2O_3), Strontium Titanate ($SrTiO_3$), and Yttria stabilized Zirconium Oxide ($Y_2O_3 - ZrO_3$) [62], [63]. In our experiments we utilized devices on $LaAlO_3$, $SrTiO_3$, and MgO substrates which are explained in more detail below. In this thesis we mainly focus on the results from $LaAlO_3$, $SrTiO_3$ based devices.

	Substrate		
	$LaAlO_3$	$SrTiO_3$	MgO
Crystal Structre	Rhombohedral	Cubic	Cubic
Lattice Parameter[a,b] (Å)	a=3.79, c=13.11	a=3.9	a=4.216
Thermal Conductivity[c,d] (W/K cm)	0.16, 0.32	0.56	3
Specific Heat[c] (J/K cm^3)	0.59	0.43	0.53
Thermal Expansion Coeff.[a] (10^-6)	9.2	10.4	12.8
Density[a,b] (g/cm^3)	6.51	3.58	3.58
Melting Point[a,b] (Celsius)	2180	2080	2800
Reflectance @ 850nm[e] (%)	8.5	15	3
Transmittance @ 850nm[e] (%)	69	73	89.5
Absorption @ 850nm[e] (%)	22.5	12	7.5

a From [63], b From [64], c From [2], d From [3], e From [27]

Table 1.1: Typical properties of single crystal 1 mm thick $LaAlO_3$ and $SrTiO_3$ substrates. Note that the values vary depending on the fabrication process techniques.

Crystalline $LaAlO_3$ has a good lattice match with YBCO to within ∼1% and can be grown to reasonably large sizes. YBCO films on $LaAlO_3$ have T_c of about 90 K and J_c of about 10^6 A/cm^2 similar to that of $SrTiO_3$. Unlike this substrate, $LaAlO_3$ is generally heavily twinned due to its structural phase transitions as shown in Figure 1.3. While heating $LaAlO_3$ wafers to the deposition temperatures of YBCO, (∼ 800°C) motion, formation, and annihilation of these twins are observable. These phenomena can cause strain and defects on the overlaying films [65]. Speculated artifacts of this property on the thermal crosstalk will be explained in Section 3.5.

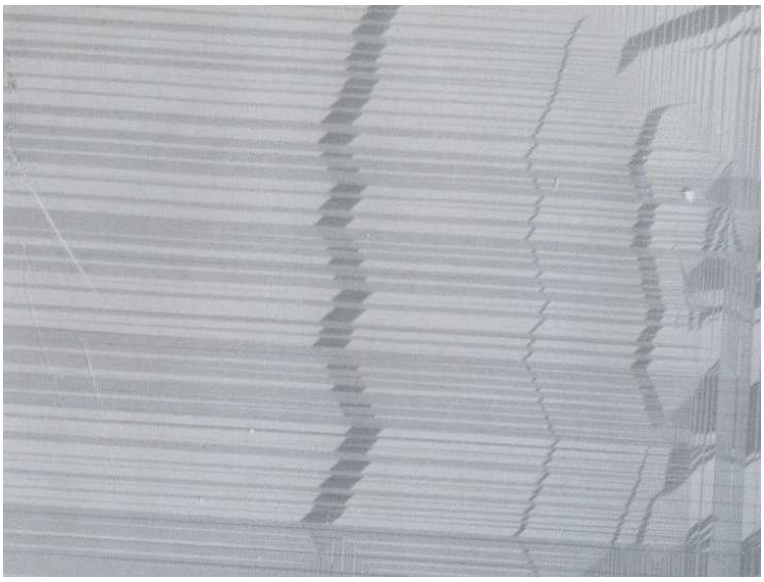

Figure 1.4: 50X magnification photo of $LaAlO_3$. The twinning in $LaAlO_3$ is seen. (Photo by Rizwan Akram.)

The thermal conductivities and thermal capacitances of $SrTiO_3$ and $LaAlO_3$ materials are close to each other as shown in Table 1.1. $LaAlO_3$ has more absorption than $SrTiO_3$ in the near IR range. The dependence of the crosstalk on the IR absorption will be explained in Section 3.4.

Knowing the above properties of these substrates, one can choose one of the substrates for optimum designs depending on the application purpose.

1.4 Thermal Diffusion Equation

Heat propagation in the crystal substrate of the devices can be considered as a conventional thermal diffusion. Numerical and analytical 3D heat diffusion process in a generic crystal has already been formulated by a number of researchers [66]–[69]. However, the solutions proposed in these studies does not take into account the phonon spectrum of the superconducting thin film on top of the substrate material. We speculated that the change of the phonon spectrum of the YBCO thin film affects the heat diffusion process in the substrate [23], [70], [71].

For our proposed analytical thermal model, we handled the heat propagation in three main parts, which is explained in details in Chapter 4. For the first part, the 1D fundamental heat diffusion equation is used. As shown below, we determine the crosstalk based on the diffusion at the surface of the substrate [7], [72], [73].

In the following, we show the derivation of the 1D lateral heat diffusion equation starting from the fundamental heat diffusion equation [74], [75].

$$\nabla^2 T - \frac{1}{D}\frac{\partial T}{\partial t} = 0 \tag{1.1}$$

Where T is temperature, $D = k_s/c_s$ and k_s and c_s are the thermal conductivity and the heat capacity of the substrate material, respectively. Assuming heat propagation only in x direction, we let $\nabla^2 = \frac{d^2}{dx^2}$. Then, we get

$$\frac{d^2 T}{dx^2} - \frac{1}{D}\frac{\partial T}{\partial t} = 0 \tag{1.2}$$

In phasor notation, we get the following equation:

$$\frac{d^2 T}{dx^2} - \frac{1}{D} j\omega T = 0 \tag{1.3}$$

Equation 1.3 is an ordinary second order differential equation, and its solution is as the following:

$$T = k_1 e^{(-1)^{1/4}\sqrt{\frac{\omega}{D}}x} + k_2 e^{-(-1)^{1/4}\sqrt{\frac{\omega}{D}}x} \tag{1.4}$$

Since $(-1)^{1/4} = \frac{1+j}{\sqrt{2}}$, k_1 should be zero for $x > 0$. Thus, we get the following solution for the temperature at the surface of the substrate:

$$T = T_0 e^{-(\frac{1+j}{\sqrt{2}})\sqrt{\frac{\omega}{D}}x} = T_0 e^{-\sqrt{\frac{\omega}{2D}}x} e^{-j\sqrt{\frac{\omega}{2D}}x} \tag{1.5}$$

The magnitude and phase of the Equation 1.5 are as the following respectively:

$$\begin{aligned} |T| &= T_0 \exp(-\sqrt{\tfrac{\omega}{2D}}x) \\ \angle T &= -\sqrt{\tfrac{\omega}{2D}}x \end{aligned} \tag{1.6}$$

In Chapter 4, this solution will be applied to the bolometer arrays for simple design purposes. Later, the model will be improved to make advanced designs to be able to explain the observed crosstalk behaviors.

1.5 Thermal Diffusion Length, L_f

As derived in Equation 1.6, as the distance from the bolometer, x, increases the magnitude of the response, $|T|$, decreases. At some x value $\ln(|T_x|)$ becomes half of the $\ln(|T_0|)$. This x value is called the thermal diffusion length, L_f, for that material and modulation frequency. By using the L_f definition and Equation 1.6, thermal diffusion length can be derived as;

$$L_f = (\frac{D}{\pi f})^{1/2} \tag{1.7}$$

Instead of finding the thermal diffusion length for a given modulation frequency, we may need to find the modulation frequency at which the substrate thickness, t_s, is equal to the thermal diffusion length. This frequency is called the knee frequency, f_L, for that substrate material and thickness. It is given by [71]:

$$f_L = \frac{D}{\pi t_s^2} \tag{1.8}$$

Physically, the thermal diffusion length, L_f, represents the characteristics penetration depth of the temperature variation into the substrate. More specifically, let the thickness of the substrate be L and then the frequency associated to this

thickness would be f_L (knee frequency) according to Equation 1.7. If the modulation frequency, f_m, of the device is above f_L, then the AC heat flow into the substrate will not reach the substrate/holder interface. In Table 1.2, the knee frequencies for 1 mm thick, single crystal substrates are shown.

Substrate	D (cm^2/s)	$f_{L=1mm}$	$f_{L=0.5mm}$
MgO	5.66	180 Hz	720 Hz
$LaAlO_3$	0.55	17.5 Hz	70 Hz
$SrTiO_3$	0.12	3.85 Hz	15.4 Hz

Table 1.2: The knee frequencies for 1 mm and 0.5 mm thick, single crystal substrates.

For example, if the modulation frequency of the IR radiation is 100 Hz, the response of two identical bolometers made on 0.5 mm or 1 mm thick $LaAlO_3$ substrate, will be very similar due to the above arguments.

1.6 Analytical Model for Single Pixel Bolometers

We have investigated and modeled the response of a single pixel bolometer in the authors MS thesis [27]. For the sake of completeness and conceptual background we will provide a summary of the model here. The model uses the electrical analogy to the thermal parameters. The electrical analogous of the thermal parameters are given in Table 1.3 [27].

Thermal Parameter	Electrical Analog
Heat Energy (Joule)	Charge (Coulomb)
Heat Flow (Watt)	Current (Ampere)
Temperature (Kelvin)	Voltage (Volt)
Thermal Impedance (Kelvin/Watt)	Impedance (Ω)
Thermal Conductance (Watt/Kelvin)	Conductance ($1/\Omega$)
Heat Capacity (Joule/Kelvin)	Capacitance (Farad)

Table 1.3: Electrical analogous of thermal parameters used in modeling the heat propagation.

A one dimensional thermal model associated to the characterization setup is shown in Figure 1.5. In this model, R_{fL} is the film lateral thermal resistance due to conduction through the YBCO to the contact areas, C_f is the film thermal capacitance, R_{fs} and R_{sc} are the film/substrate and substrate/cold-head thermal boundary resistances and R_s and C_s are the substrate thermal resistance and capacitance respectively. While the first four parameters can be used as a lumped circuit element in the model, the latter two cannot be used. Thus, in order to find the thermal impedance seen from the surface of the film, we should find the thermal impedance of the substrate. We can do this by using the analogy between a transmission line and the substrate. If we divide the substrate into infinitesimally small segments, one of which is shown in Figure 1.6, a substrate segment of thickness Δx can be modeled with a simple RC circuit. The resistance of the segment is calculated by $r(x)\Delta x$ where $r(x)$ is the unit length resistance at position x and the capacitance is calculated with $c(x)\Delta x$, where $c(x)$ is the unit length capacitance at position x. Similar approach as finding the delay in a VLSI wire in [76] is used for finding the substrate thermal impedance.

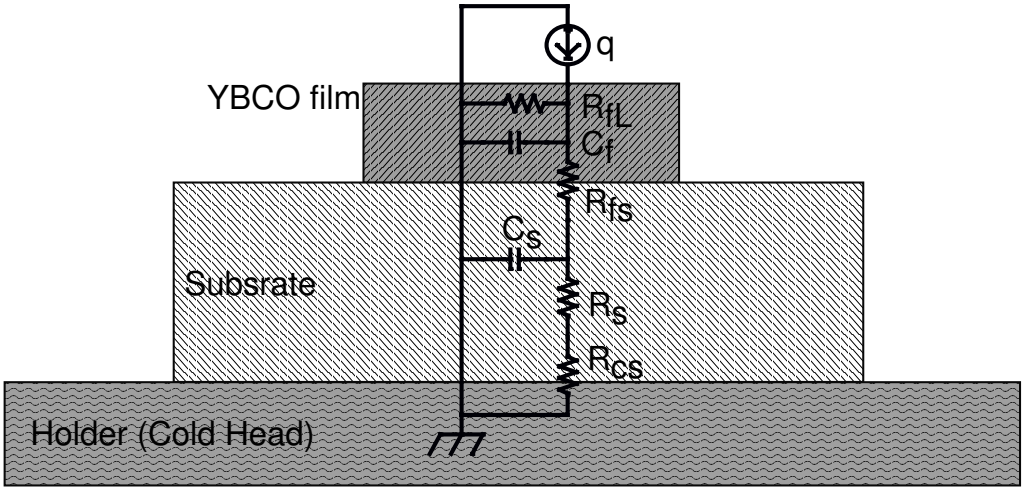

Figure 1.5: Electrical analog of the thermal model and source for each parameter. The physical dimensions are not to scale.

The equilibrium equations of the circuit, by Kirchoff's voltage and current laws, are

$$v(t, x + \Delta x) - v(t, x) = -r(x)\,\Delta x\, i(t, x + \Delta x) \tag{1.9}$$

$$i(t, x + \Delta x) - i(t, x) = -c(x)\,\Delta x\,\frac{\partial v(t, x + \Delta x)}{\partial t} \tag{1.10}$$

In the limit that $\Delta x \to 0$, we get the following PDEs,

$$\frac{\partial v(t, x)}{\partial x} = -r(x)\, i(t, x) \tag{1.11}$$

$$\frac{\partial i(t, x)}{\partial x} = -c(x)\,\frac{\partial v(t, x)}{\partial t} \tag{1.12}$$

If we take the Fourier transform, we have

$$\frac{\partial V(\omega, x)}{\partial x} = r(x)\, I(\omega, x) \tag{1.13}$$

$$\frac{\partial I(\omega, x)}{\partial x} = -j\omega c(x)\, V(\omega, x) \tag{1.14}$$

By using the above equations,

$$\frac{\partial^2 V(\omega, x)}{\partial x^2} = j\omega\, r(x)\, c(x)\, V(\omega, x) + \frac{1}{r(x)}\frac{dr(x)}{dx}\frac{dV(\omega, x)}{dx} \tag{1.15}$$

$$\frac{\partial^2 I(\omega, x)}{\partial x^2} = j\omega\, r(x)\, c(x)\, I(\omega, x) + \frac{1}{c(x)}\frac{dc(x)}{dx}\frac{dI(\omega, x)}{dx} \tag{1.16}$$

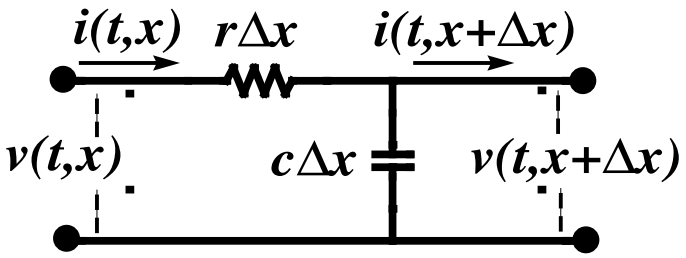

Figure 1.6: Circuit analog of a substrate segment Δx. $r\Delta x$ and $c\Delta x$ are segment resistance and capacitance. r and c are the unit length resistance and capacitance respectively.

We can solve these equations using Mathematica^{TM} for arbitrary r(x) and c(x) and we get the impedance matrix Z_{sub}:

$$\begin{bmatrix} V(0) \\ V(l) \end{bmatrix} = \underbrace{\begin{bmatrix} z_{11} & z_{12} \\ z_{21} & z_{22} \end{bmatrix}}_{Z_{sub}} \begin{bmatrix} I(0) \\ I(l) \end{bmatrix}$$

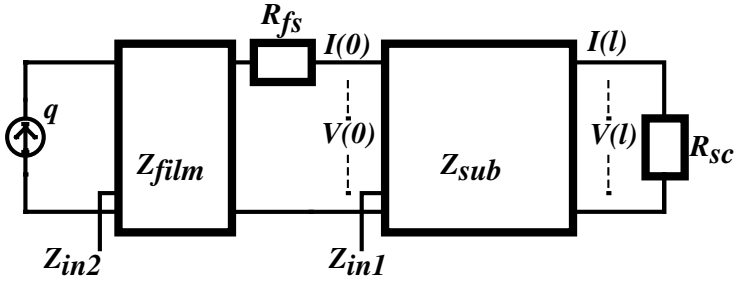

Figure 1.7: Impedance matrix for the holder configuration used in the analysis

In above, $Z_{film} = \frac{R_f}{1+j\omega C_f R_f}$ from basic RC circuit, and we can calculate Z_{in1} as in Equation 1.17 from the two port model terminated by Z_{sc} [77].

$$Z_{in1} = z_{11} + \frac{z_{12} * z_{21}}{R_{sc} - z_{22}} \tag{1.17}$$

Thus we get Z_{in2} as follows:

$$Z_{in2} = \frac{Z_{film} * (R_{fs} + Z_{in1})}{Z_f + R_{fs} + Z_{in1}} \tag{1.18}$$

Finally, $q * Z_{in2}$ gives the voltage (=temperature) of the film.

For large area patterns, we can use unilateral heat propagation and consider the propagation area equal to the film area, A, throughout the substrate. Then we get, $r(x) = r_s/A = 1/(k_s * A)$ and $c(x) = c_s * A$. For these values of $c(x)$ and $r(x)$, we get the substrate impedance matrix Z_{sub} as follows:

$$Z_{sub} = \frac{1}{\sqrt{j\, c_s\, k_s\, \omega}} \begin{bmatrix} \coth(\gamma\, l) & -\mathrm{csch}(\gamma\, l) \\ \mathrm{csch}(\gamma\, l) & -\coth(\gamma\, l) \end{bmatrix} \tag{1.19}$$

where,

$$\gamma = \sqrt{\frac{j\omega c_s}{k_s}} \tag{1.20}$$

We get Z_{in1} and Z_{in2} by using equations 1.17 and 1.18 as follows, same as reported in reference [78] as a steady state solution to a general one-dimensional heat propagation equation, neglecting R_f.

$$Z_{in1} = \frac{e^{(\gamma\ell)} + \Gamma e^{-\gamma\ell}}{e^{(\gamma\ell)} - \Gamma e^{-\gamma\ell}} \sqrt{\frac{1}{j\omega c_s k_s}} \tag{1.21}$$

$$Z_{in2} = \frac{\frac{e^{(\gamma\ell)} + \Gamma e^{-\gamma\ell}}{e^{(\gamma\ell)} - \Gamma e^{-\gamma\ell}} \sqrt{\frac{1}{j\omega c_s k_s}} + R_{fs}}{\frac{e^{(\gamma\ell)} + \Gamma e^{-\gamma\ell}}{e^{(\gamma\ell)} - \Gamma e^{-\gamma\ell}} \sqrt{\frac{j\omega}{c_s k_s}} C_f + 1 + j\omega C_f R_{fs}} \tag{1.22}$$

where,

$$\Gamma = \frac{R_{sc} - \sqrt{\frac{1}{j\omega c_s k_s}}}{R_{sc} + \sqrt{\frac{1}{j\omega c_s k_s}}} \tag{1.23}$$

1.7 Previous Crosstalk Studies

In 2001, Gaugue *et al* [11] has investigated the substrate influence on inter-pixel crosstalk in the YBCO mid-infrared bolometers and proposed 2D analytical and 3D numerical models. He has concluded that "the 2D model can be used to predict the optical response for the illuminated pixel but ceases to be valid to be used for the optical response of the non-illuminated adjacent pixel. So, interpixel crosstalk has to be evaluated only by a 3D model and the thermal interface must be taken into account." However, 3D numerical model was able to explain the thermal crosstalk up to mid-modulation frequencies, where the thermal crosstalk starts to cease and the leaking input laser response starts to dominate as shown in Figure 1.8.

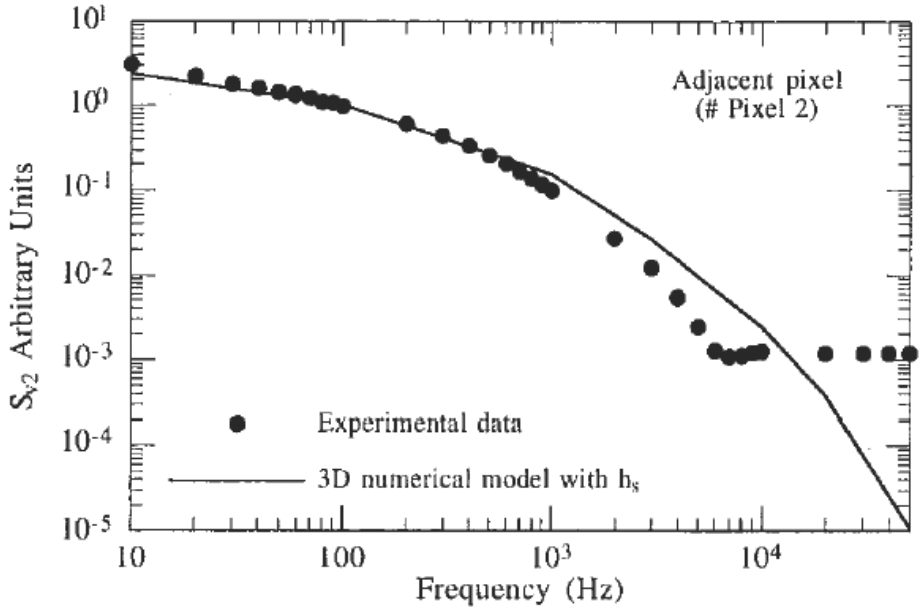

Figure 1.8: 3D numerical model calculation results and experimental data from Gauge *et al* [11].

In 2003, Delerue *et al* has reported the thermal crosstalk measurement results on YBCO Mid-Infrared Bolometer Arrays. They have defined some key parameters in the interpixel thermal crosstalk such as the corner frequencies in the response of the neighbor pixels and detectivity in the bolometer arrays. They have also reported the response vs. laser spot position for testing the imaging

performance of the array. They have not used a reflecting mask on the non-illuminated pixels and they have not used gold coated contact pads. Thus, their crosstalk measurement results, especially in the high frequency ranges, had some artifacts due to the optical response of the YBCO pads where not only the source pixel is illuminated but also the sense pixel was illuminated. The results from our devices used in this thesis is protected against the above artifacts by the special engineering of the device structure explained in the following chapters.

Chapter 2

Fabrication Of The Bolometers and Characterization Setup

2.1 Sample Preparation

The devices used in this study were made of 200 nm and 400 nm thick c-axis oriented YBCO films on 0.5 - 1 mm thick substrates deposited by pulsed laser deposition (PLD) at Julich Research Center - Germany [70]. For more details of the PLD process, the reader is encouraged to read the references [79]–[81].

On top of the superconducting films we prepared 4×1 bolometer arrays to investigate the thermal coupling or the crosstalk between the devices in the form of arrays of long bridges. The illuminated device in the array had an area of 20 μm × 1 mm and the neighboring test devices had areas of 20 μm × 0.75 mm. In order to measure the crosstalk between the devices, it is essential to keep the test bolometers optically isolated from the environment. However, it was further taken into consideration that optically isolating the devices does not cause additional thermal coupling artifacts in the array. The details of the array and mask are explained in the following section.

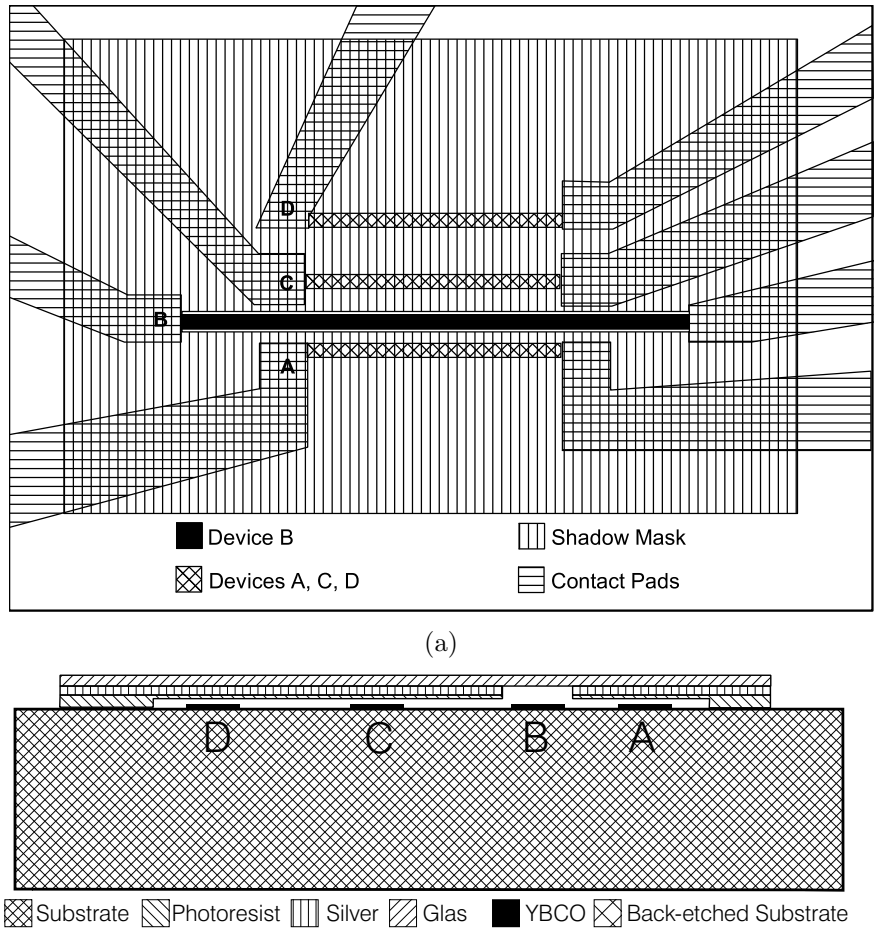

Figure 2.1: Top (a) and side (b) view of the test devices. The illuminated device and the neighbor devices are shown together with the shadow mask.

The four neighbor devices of our design are shown in Figure 2.1. One bolometer, the "source-device", (named B) is illuminated with modulated IR radiation whereas the remaining three bolometers, "sense-devices", are blocked with a free standing reflecting mask. The separations of the sense-bolometers named, A, C, and D, from the source-bolometer were 40, 60, and 170 μm respectively.

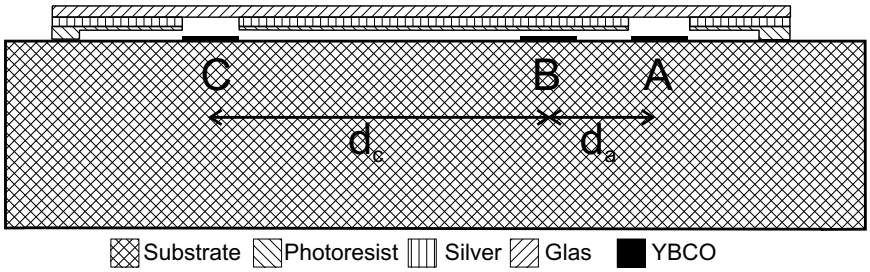

Figure 2.2: Side view of the bolometer array used in the non-contact read-out feasibility test experiments shown in Chapter 5. The read-out pixel B, and the sense-pixels A and C are shown.

2.1.1 Reflecting Mask

The radiation blocking was achieved in a flip-chip configuration. The reflecting mask was made of a 250 nm thick sputtered silver layer on 0.1 mm glass so that the IR transmittance was negligible. For silver deposition, we used Denton Vacuum Desk II etch-sputter unit with the silver target option. Then using standard lithography process, a 25 μm wide groove was opened in the reflecting layer. A 1.4 μm thick photoresist layer was spinned and a larger window was opened so that the mask was free standing on top of the devices, eliminating any parasitic thermal or electrical contacts that could affect the measurements. The oxidation problem of the silver was not faced since the top side of the silver was on the glass side and the bottom side was coated with a thick layer of photoresist.

Instead of making the mask on-chip, we preferred it to make it with the flip-chip configuration. This way, the fabrication process was much more easier and we had the flexibility of changing the mask position on different pixels and changing the number of windows in the mask for different applications. For example, in addition to the crosstalk studies, the same bolometer array has been used to test the feasibility of electrical contact free read-out of bolometer arrays by means of thermal crosstalk. For this purpose, we designed an other mask which had two windows rather than one as shown in Figure 2.2. The details of this study is presented in Chapter 5.

2.1.2 Array Preparation

The array was fabricated by using standard lithography process and chemical etching on top of the PLD films that were explained in the previous section. For chemical etching we used 0.75% H_3PO_4 acid diluted with DI water for 30 to 60 seconds depending on the thickness of the film. The contact paths and pads were coated by a sputtered gold layer so that the YBCO contact paths with nonzero resistance at the operating temperatures were shorted assuring that the generated response is only due to the bridges. The gold-deposited parts of the YBCO are shown in horizontal hatch pattern and the bridges are shown in cross hatch pattern in Figure 2.1-a. The effective lengths of the bridges facing the direct thermal coupling were 0.5 mm, so that the lateral thermal conductance dominates over the longitudinal thermal conductance of the devices. Finally, the groove was aligned and the mask was fixed on top of the source-bolometer as shown in Figure 2.1.

2.1.3 Back-etching the substrate

There is no known chemical to etch $LaAlO_3$ and $SrTiO_3$ materials. Thus, to remove the substrate-holder interface, we had to etch the bottom of the substrate by mechanical means. The problem with this solution is that, first we make the measurements without back-etching the samples then repeat the same experiment with various amounts of back-etching. Thus, while back-etching, the microbridges had to be protected against excess pressure and excess heating. The ethcing amounts were in 250 μm increments in three steps. Thus, we had to monitor the amount of exching during etching as well. To overcome all these issues, we used a small PCB driller with proper tip and a home-made setup to be able to apply the required minimum pressure and remove the generated heat during drilling. The system had a scale to monitor and measure the amount of etching as well.

2.2 Characterization Setup

The responses of the samples were measured under a DC bias current, I_{bias}, in 4-probe configuration using an automated low noise characterization setup as shown in Figure 2.4.

The temperature of the substrate was controlled with a maximum 20 mK deviation from the target temperature using a liquid nitrogen dewar (Janis VPF-475) and a software PID controller. As a temperature sensor, $Pt-500$ is used which has a linear temperature dependent resistance in lN_2-room temperature range. The sensor was calibrated by measuring the resistance in lN_2 (77.3 K) and ice water (273.7 K), and finding the linear relation between temperature and the resistance. The resistance of $Pt-500$ is measured with 4-wire resistance measurement method using Agilent 3401A DMM with 100 μA bias current to prevent self-heating. The sensor is mounted in a groove, 1 mm below the sample so that the temperature gradient is minimized. The metal film resistor heater, powered by an HP6628A DC power supply, is placed 1 cm away from the sample and can control the temperature up to 150 K with a maximum power of 5 W. For the temperatures close to 90 K, 1-2 W is sufficient and 250 ml of lN_2 provides cooling the dewar for 2 hours. The thermal conductance from the cold head to the lN_2 reservoir was intentionally decreased by adding some insulator in between so that the thermal run away from the cold head is further decreased. The temperature controller can increase or decrease the temperature of the system by up to 5 K/min. In Figure 2.3, the temperature stability of the system for a fixed and decreasing temperature is shown.

The optical response of the devices, the phase and magnitude of the devices under the IR radiation, were measured with SR850 DSP lock-in amplifier, the input of which was amplified with an ultra-low noise preamplifier (Stanford SR 570). As a radiation source, electrically modulated, fiber coupled IR laser diode with wavelength of 850 nm, and 12 mW power was used (from Power Technologies). Since the quartz window was not close enough to the sample, we used a lens to focus the light to get higher intensity without sacrificing the homogeneity of the light on the patterns.

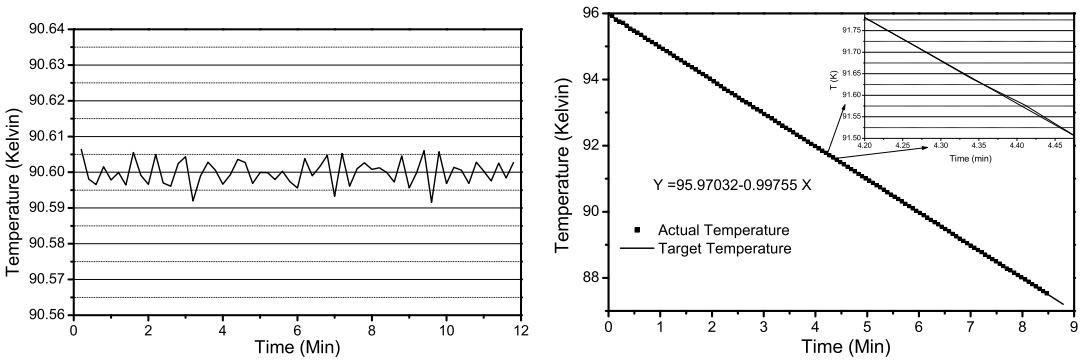

(a) (b)

Figure 2.3: Temperature (a) stability over a frequency sweep time -12 min- and (b) decrease 1K/min over a temperature sweep time -6 min-. Maximum deviation from the target temperature is less than 20 mK

The system is capable of measuring all four devices in one cooling cycle without altering the electrical or thermal contacts, or the optical setup. In all the measurements, the magnitude of the response was at least one order of magnitude greater than the system noise.

The responses of the devices were measured versus radiation modulation frequency in the range of 1 Hz to 100 KHz, limited by the lock-in amplifier. During the measurements, the temperature was fixed at three different values. First, the temperature was fixed at the middle of the superconductivity transition where the highest response magnitude was obtained (T_{c-mid}), then it was fixed above and below the T_{c-mid} to get a response magnitude approximately 10 % of the maximum. These temperature values were defined as $T_{c-onset}$ and T_{c-zero} respectively. The set of measurements were repeated for bolometers made on different substrate materials ($SrTiO_3$ and $LaAlO_3$) for films of different thicknesses (200 nm and 400 nm).

Currently, an analog switch as well an preamplification addition has been made to the system as a senior design project [82]. With this addition, the system is capable of doing the measurements without any manual interaction up to four different samples. In addition, a low temperature opamp is integrated

together with the switch so that the signal is amplified at cryogenic temperatures close to the sample before any noise is added. Since the measurements shown in this study are made with the system before the addition of the complimentary circuitry, we do not explain the details of the new configuration here.

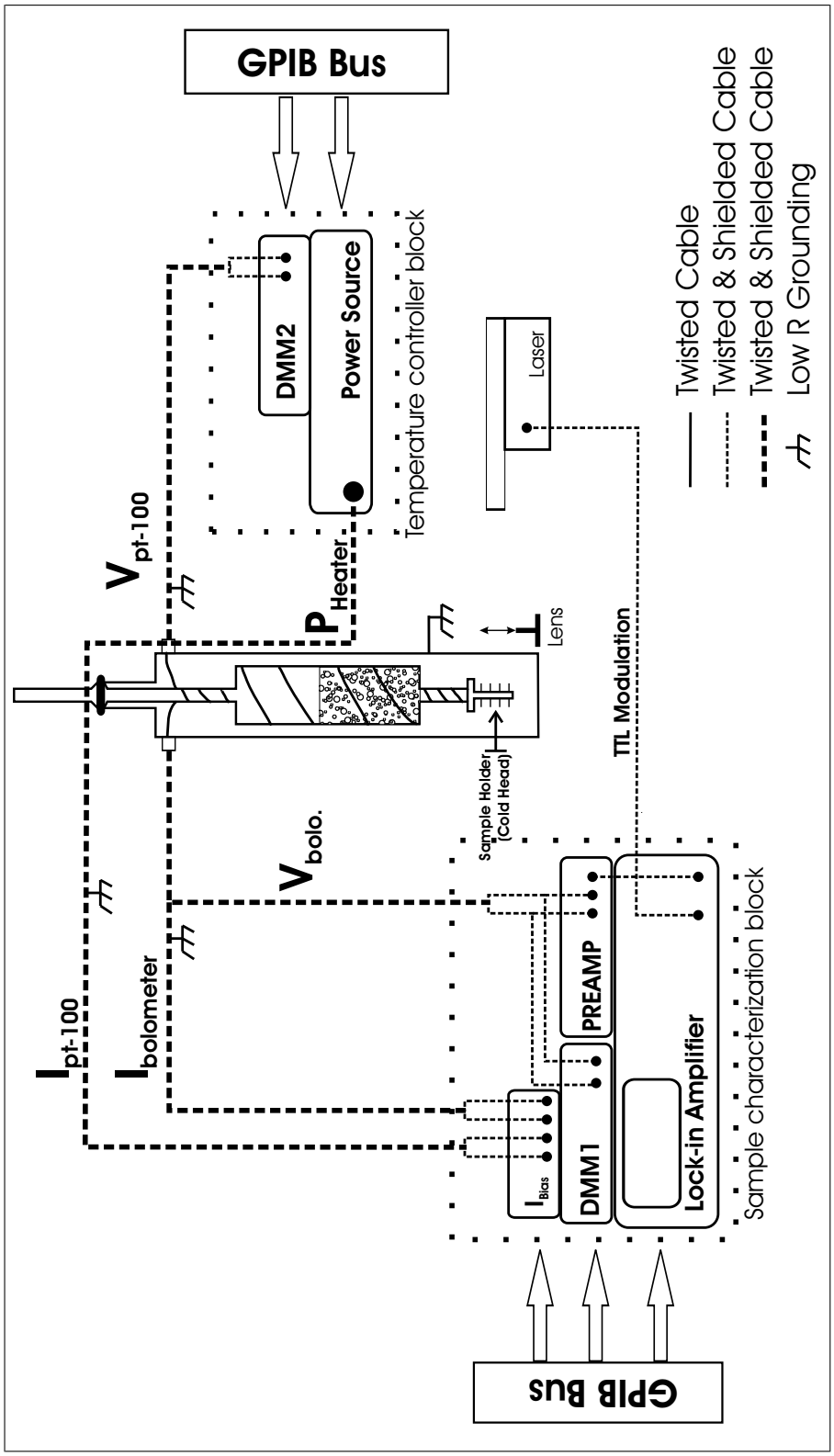

Figure 2.4: Block diagram of the characterization setup shown with electrically modulated IR laser [27].

Chapter 3

Experimental Results and Analysis

Response of the bolometers are affected by several parameters. The amount of parameters involved in the response makes the analysis complicated. However, once the operation of a bolometer is understood, each of these parameters provide us an extra degree of freedom to make optimal designs for desired response characteristics.

In this thesis, we have investigated the dependence of the response of the bolometers on various physical parameters such as the bias temperature, device separation between the neighbor pixels, substrate material, YBCO film thickness and substrate back-etching.

As explained in more detail in Chapter 2, the source pixel is illuminated and the sense response of the sense pixels were measured. The measured crosstalk response of the devices has a lag due to the diffusion in the substrate. Thus, the measured response is a complex quantity and it has both magnitude and phase as shown in Equation 4.1. The voltage responses of the sense-devices versus the radiation modulation frequency shown in this study can be divided into two main parts: the response generated due to the crosstalk between the source-device and the response generated by the leaking laser beam directly due to the imperfect

Table 3.1: The crosstalk-free modulation frequencies of devices A, C, and D at T_{c-zero}, T_{c-mid}, and $T_{c-onset}$ for $SrTiO_3$ and $LaAlO_3$ substrates.

Substrate	Device	d (μm)	Crosstalk-free f_m (Hz)		
			T_{c-zero}	T_{c-mid}	$T_{c-onset}$
$SrTiO_3$	A	40	17853	15500	-
$SrTiO_3$	C	60	7590	5850	4611
$SrTiO_3$	D	170	762	645	366
$LaAlO_3$	A	40	69400	34870	-
$LaAlO_3$	C	60	13840	8730	-
$LaAlO_3$	D	170	1743	1100	-

blocking of the radiation by the reflecting shadow mask.

For example, the response of the device D in Figure 3.1 is due to the crosstalk up to about 700 Hz and mainly due to the direct absorption of the leaking laser beam after about 2.5 kHz. As observed in Figure 3.1, the phase and magnitude behavior of the response of device D are the same as the source-device B for $f \geq$ 2.5 kHz. For device D, which is separated by 170 μm distance, the crosstalk-free modulation frequency is around 1 kHz. Above this frequency, the coupling is expected to become negligible and the unblocked leaking input laser power, in the order of 1%, starts to dominate the measured response. As observed in Figure 3.1-b, the magnitude of the response of device D at higher frequencies ($f \geq 10$ kHz) is approximately two orders of magnitude smaller than that in device B, which shows that the radiation blocking of the shadow mask is more than 99%.

The modulation frequencies between 700 Hz and 2.5 kHz, lead to a mixed and complicated response behavior. This is because the response due to the crosstalk and the leaking laser beam through the shadow mask become comparable in this range. The phase and magnitude depths of the responses at above the knee frequency of the curves in Figure 3.1 are associated with the interference of the responses due to the leaking laser beam and the thermal crosstalk from the source-device. This is investigated and explained in detail in Chapter 4 by using the proposed analytical thermal model. Here we have analyzed the crosstalk

based responses of the devices qualitatively by considering them from five main aspects: i) the effect of the separation between the devices, ii) superconductivity transition, iii) substrate material, iv) back-etching of the substrate, v) the YBCO film thickness on the crosstalk characteristics.

3.1 Effect of separation between the devices on the crosstalk based response

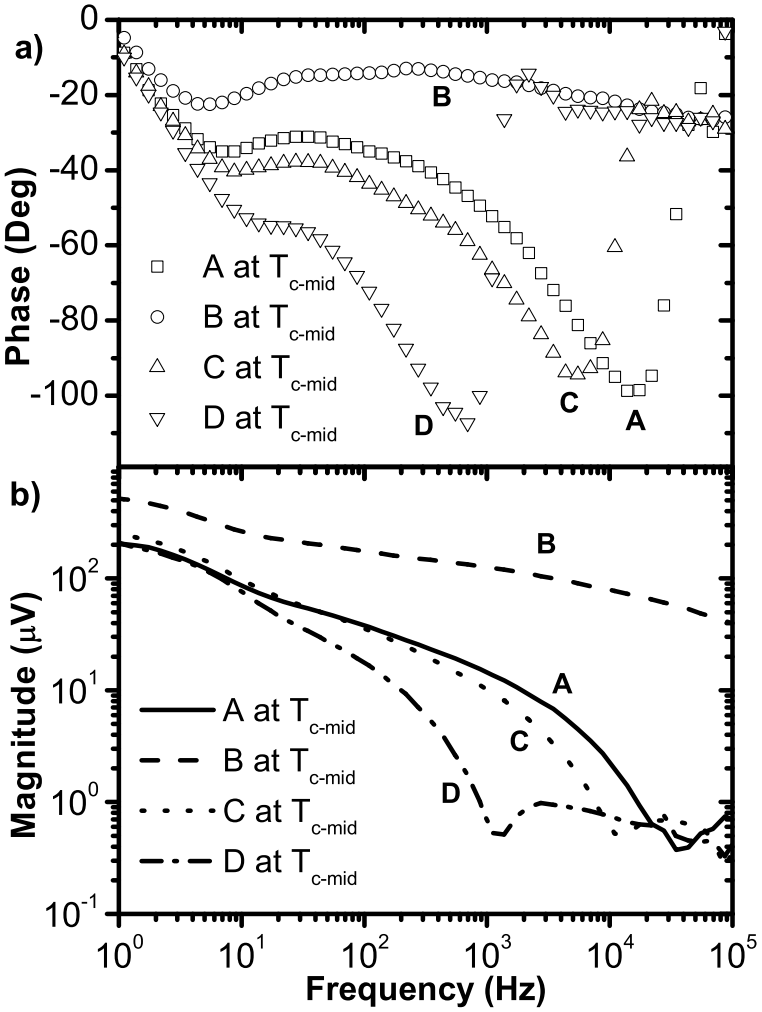

Figure 3.1: Phase (a) and magnitude (b) of the IR response vs. frequency of bolometers A, B, C, and D on 1 mm thick $SrTiO_3$ substrate at T_{c-mid}. The effect of the separation distance on the response is clearly observed.

The dependence of the response on the separation between the devices is shown in Figure 3.1 for devices on a 1 mm thick $SrTiO_3$ substrate. The thermal diffusion length, that represents the characteristic penetration depth of the temperature variation into the substrate, as explained in Section 1.5, is found from:

$$L_f = \sqrt{\frac{D}{\pi f}} \tag{3.1}$$

Where T_0 is the temperature at x=0, f is the modulation frequency, $D = k_s/c_s$ is the thermal diffusivity of the substrate material, and k_s and c_s are the thermal conductivity and the specific heat of the substrate materials, respectively [72]. For example, the thermal diffusion length for the $SrTiO_3$ substrate at 4 Hz would be 1 mm, the thickness of the substrate.

At low frequencies, all the characterized neighbor devices behaved the same, as shown in Figure 3.1. That is, their response magnitude behaviors and phases are very close to each other. This is interpreted to be caused by the fact that the thermal diffusion length in this range is comparable to the substrate thickness leading to an almost similar temperature variation for all the neighbor devices. In this range of frequency, the Kapitza boundary resistance is the dominant thermal parameter affecting the response [70], [71] and all the devices behave as if they are perfectly coupled to each other. As the thermal diffusion length starts to be comparable to the distance between the devices, the response curves start to diverge from each other. Eventually, after the modulation frequency becomes high enough to cease the coupling, the devices again converge to the response of the input device, B, due to the leaking laser beam as discussed earlier. Thus, for each device at different temperatures we can define a modulation frequency after which the crosstalk is negligible. The crosstalk-free modulation frequency values in Table 3.1 have been obtained by getting the phase minima versus modulation frequency for devices A, C, and D. Above these frequency values, the crosstalk is negligible and the response is only generated by the leaking input laser itself. For example, the values of the 4^{th} column in Table 3.1 are found from the frequencies where the minimum phase occurs in the curves in Figure 3.1-a. After these frequencies, the crosstalk can be considered to be negligible compared to the leaking laser term.

3.2 Effect of Superconductivity Transition on the response behavior of the samples

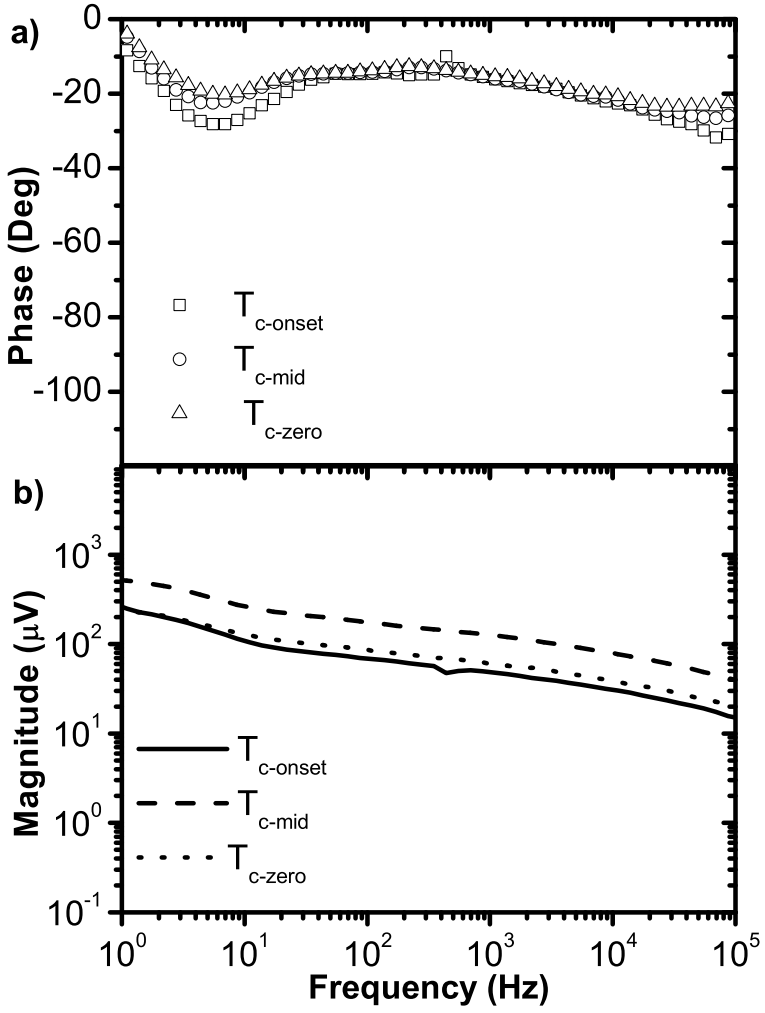

Figure 3.2: Phase (a) and magnitude (b) of the IR response vs. frequency of the source bolometer, B on 1 mm thick $SrTiO_3$ substrate. The data is taken at three different temperatures: T_{c-zero}, T_{c-mid}, and $T_{c-onset}$.

One of the immediate observations in the response of the devices is a strong temperature dependence of the phase of the source-devices at low modulation frequencies, f_m, as shown in Figures 3.2 and 3.3. This has been explained for small and large area single pixel devices in [70] and [71]. There was discussed that the transition-dependent change of the phase of the response is due to the effects of the order parameter of the YBCO material on the phonon spectrum, which also

determines the Kapitza boundary resistance. Since the thermal diffusion length at low modulation frequencies is greater than the device separation, the sense-devices are also strongly coupled to the source-device in this range of frequencies.

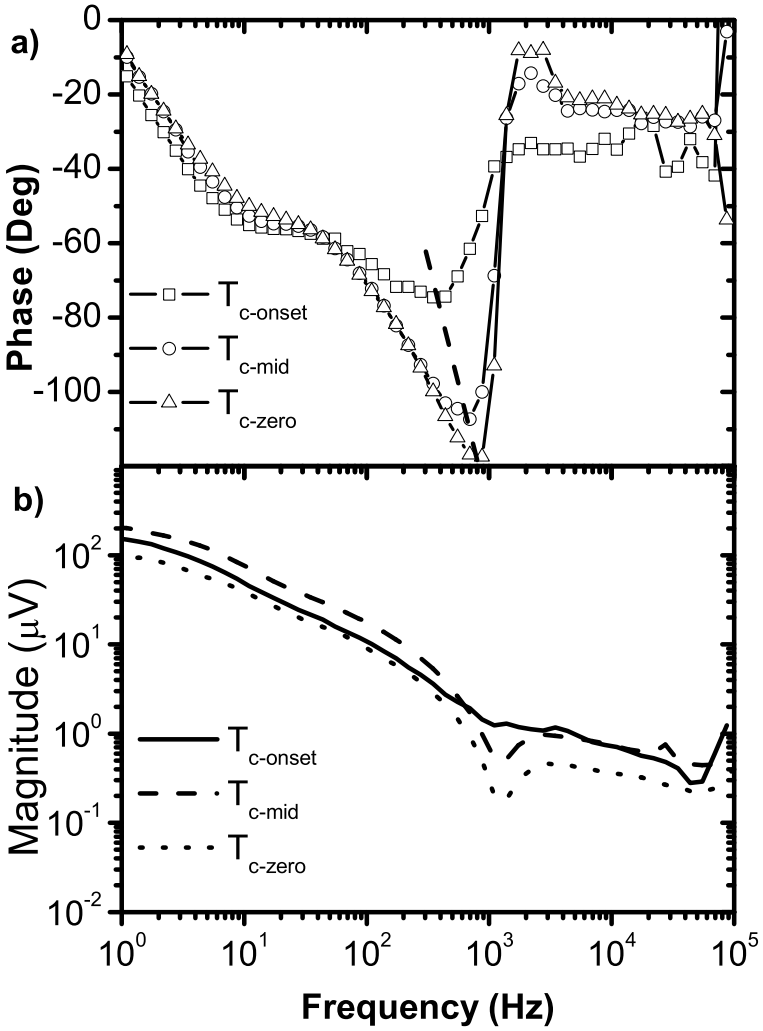

Figure 3.3: Phase (a) and magnitude (b) of the IR response vs. frequency of the sense bolometer, D on 1 mm thick $SrTiO_3$ substrate. The data is taken at three different temperatures: T_{c-zero}, T_{c-mid}, and $T_{c-onset}$.

We have also measured the response in the illuminated device without a shadow mask to verify the above result, compared to the previously reported results on the large area devices. As measured, the response of the device B did not change considerably compared to that of the shadowed case. Temperature

dependent response of a single device has been reported elsewhere [70], [71]. The response behavior in Figure 3.2 is also affected by the gold deposition over the contact paths, the effects of which dominate the temperature dependence of the other thermal parameters in the device such as the lateral thermal conductance through the YBCO film or the film-substrate thermal resistance.

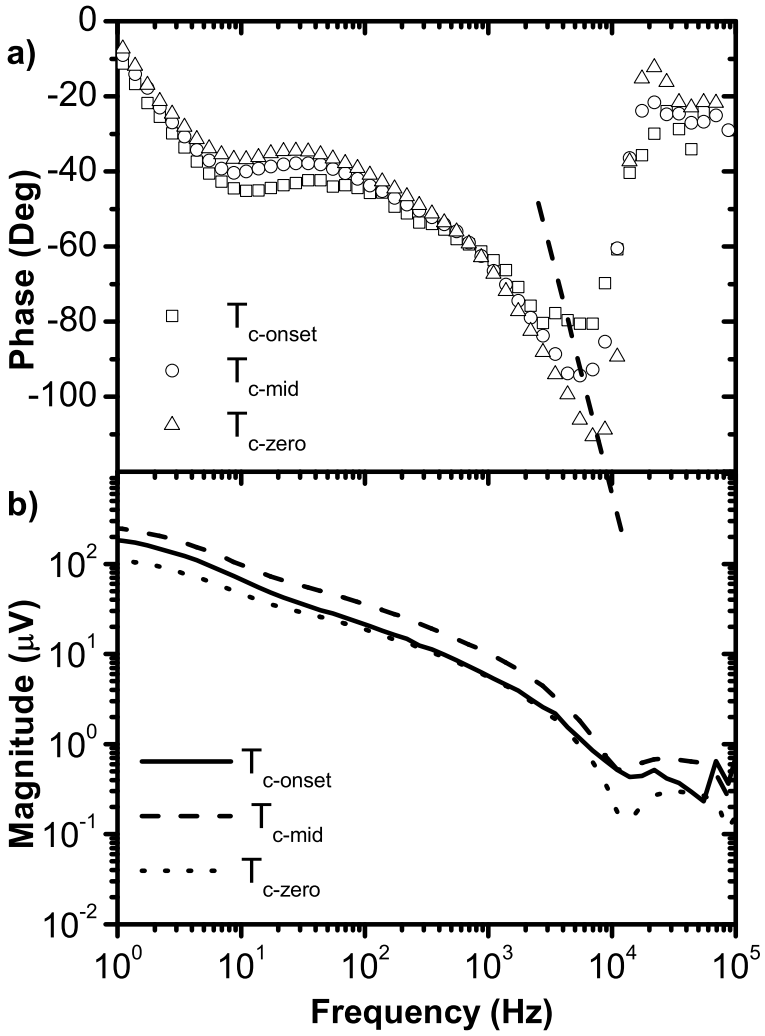

Figure 3.4: Phase (a) and magnitude (b) of the IR response vs. frequency of the sense bolometer, C on 1 mm thick $SrTiO_3$ substrate. The data is taken at three different temperatures: T_{c-zero}, T_{c-mid}, and $T_{c-onset}$.

As shown in the Figure 3.2, the response of the source-device B does not show considerable temperature dependence. However, Figures 3.3 and 3.4 show that the responses of devices C and D are strongly dependent on the superconductivity

transition. Similar temperature dependent results have also been obtained for device A. Thus, the strong temperature dependent response of the devices A, C, and D are associated to be caused mainly by the superconductivity transition dependent crosstalk between the devices.

Using the phase of the response of device D in Figure 3.3, the crosstalk-free modulation frequency at $T_{c-onset}$ is lower than that of T_{c-zero}. Based on the above, the coupling between the devices is found to be more at lower temperatures, enabling crosstalk at higher frequencies. By using these crosstalk modulation frequencies and the proposed thermal model in Section 4.1, the lateral thermal diffusivity values are obtained and given in Table 4.2.

3.3 Effect of the thickness of the YBCO Film

Based on the measured crosstalk-based response of the 200 nm and 400 nm thick YBCO film bolometers with designs as shown in Figure 3.5, film thickness is found to affect the response at both low and high modulation frequency ranges. For clarity, the data in Figure 3.5 (except for pixel D made of 200 nm thick YBCO film) are plotted just up to the lowest points, where the response starts to be dominated by the direct absorption of the leaking laser beam.

We observed that the phases of the response of the 400 nm thick film bolometers were smaller and the rates of decrease of magnitude versus frequency were slower than those of the thinner film bolometers. Thus, as shown in Figure 3.5, there was more crosstalk between the bolometers made of thick films. We associate this to the ratio between absorption of IR radiation by the YBCO thin film and by the substrate. The 400 nm YBCO films absorb more radiation than the 200 nm films; the lag which is possibly caused by the substrate material, is decreased in the thicker film samples. The confirmation of this result based on the analytical thermal model is provided in Section 4.3.3.

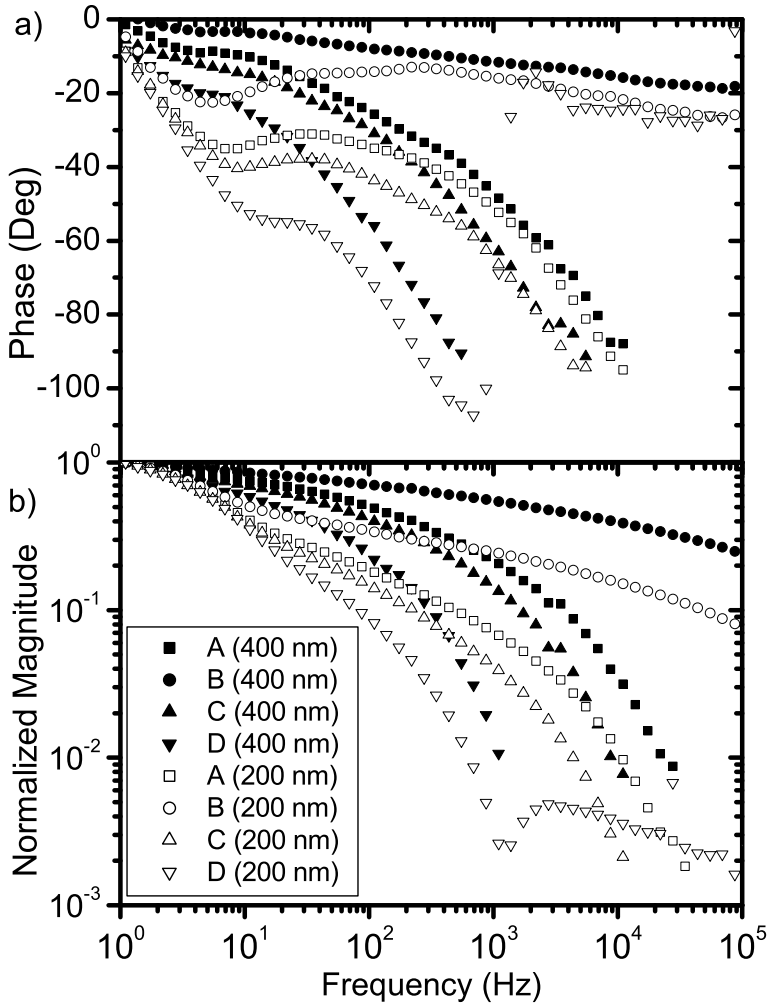

Figure 3.5: a) Phases and b) magnitudes of 200 nm thick devices and 400 nm thick devices.

There are two issues to consider when fabricating bolometers using thick films. As the cross sectional area through which the current passes increases, electrical resistance decreases, decreasing dR/dT. Second, as the film thickness is increased, beyond about 300 nm in our PLD system, YBCO film quality decreases and hence the superconductivity transitions of the thick films were less sharp than the thinner ones. The loss in the sharpness of the transition with the thicker films might be avoided by optimizing the PLD system, but the inherent decrease in resistance of the film due to the thicker film would result in an overall lower dR/dT degrading the response.

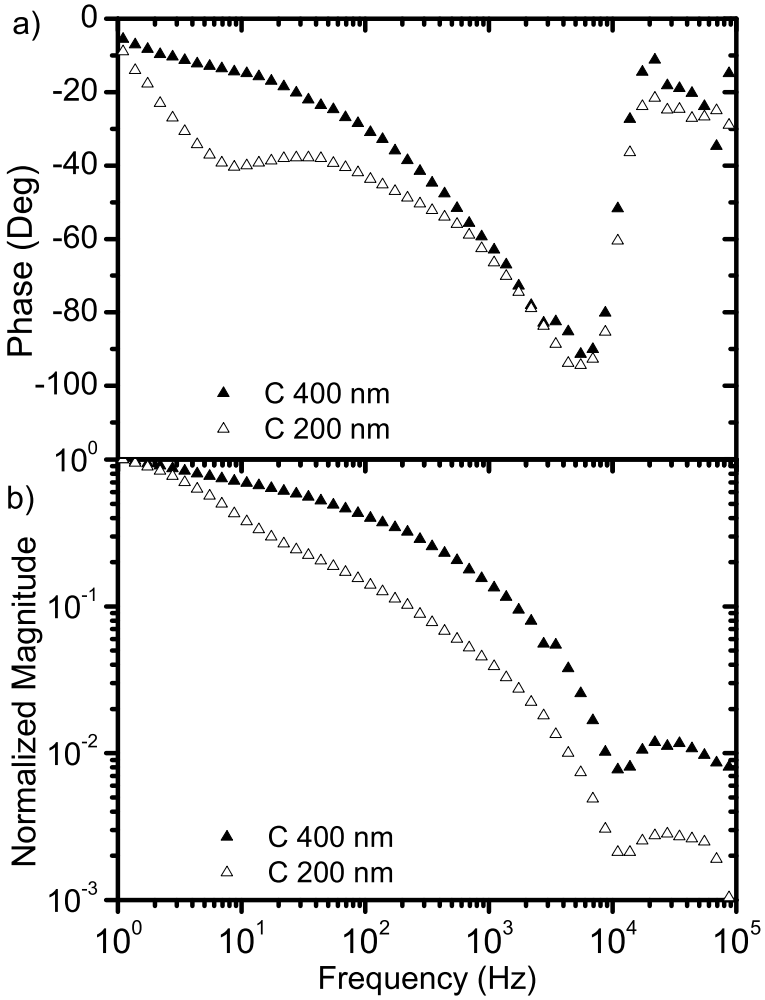

Figure 3.6: a) Phases and b) magnitudes of 200 nm and 400 nm thick devices and their fitting curves.

In [83], we investigated the effect of the transition width and film quality of the YBCO films on the response of a single pixel bolometer. We observed that as the transition width increases, the phase dip at low frequencies decreases due to the difference of the lateral thermal conductivity of the YBCO film. However for the purpose of this study, we have coated the contact paths of the bolometers with gold; this dominated over the thermal parameters of the film and we did not observe the phase dip at low frequencies that happened with the low quality films in [83]. We can only interpret that the difference in the crosstalk-based phase of the response is not associated with the transition width of the films. Crosstalk characteristics of the bolometers based on thicker films are mainly interpreted

to be due to differences in absorbtivities of the 200 nm and 400 nm YBCO films. Possible effects of structural film quality on the crosstalk has not been investigated.

The decision about the optimal thickness of the YBCO films should be with the consideration of the thickness dependence of the film quality, the dimensions of the bolometers, and the targeted range of the operation modulation frequency.

3.4 Effect of the Substrate Material

The thermal diffusivity of the substrate material is one of the fundamental parameters that affect the thermal crosstalk between the pixels in an array. This is especially true at the low and mid ranges of the modulation frequencies, f_m, where the thermal diffusion length is in the same range as the substrate thickness. In this range, the substrate thermal conductance and thermal capacitance become the dominant parameters, which affect the response of the bolometers [70].

Figure 3.7 shows the crosstalk response vs. frequency curve of pixel C on $LaAlO_3$ and $SrTiO_3$ substrates. The crosstalk-free f_m for pixel C on $LaAlO_3$ is 21927 Hz whereas the crosstalk-free f_m for pixel C on $SrTiO_3$ substrate is 5850 Hz. Based on these frequencies, the lateral thermal diffusivities of the $LaAlO_3$ and $SrTiO_3$ are calculated to be 0.088 and 0.027 cm^2/s, respectively in Section 4.1.

In this study, we did not investigate the effect of substrate thickness on the crosstalk between the pixels. However, based on previously reported single pixel studies [70], [71], as the thickness of the substrate decreases, the thermal diffusion length becomes comparable to the thickness of the substrate at higher frequencies as shown in (3.1), and the Kapitza boundary resistance affects the response for a higher ranges of frequencies. For example, in Figure 3.7-a, the knee point around 4 Hz, caused by Kapitza boundary resistance, is clearly seen in the phase vs. frequency plot of $SrTiO_3$. Based on (3.1), as the thickness is decreased, the knee

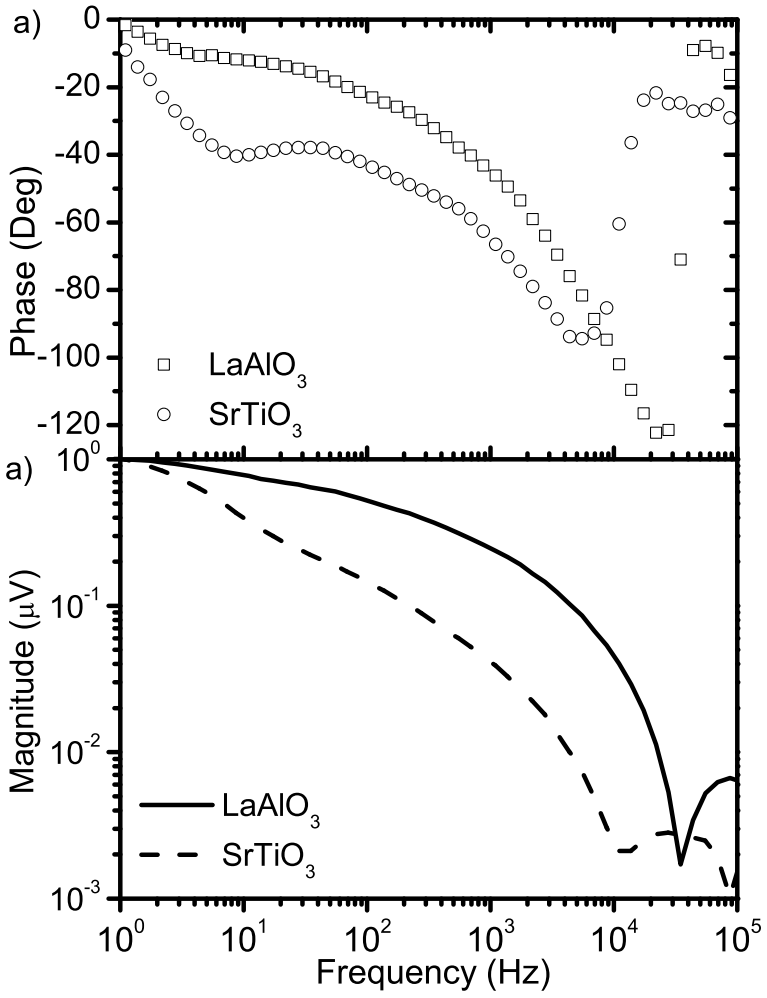

Figure 3.7: a) Phases and b) magnitudes of devices C on $LaAlO_3$ and $SrTiO_3$ substrates and their fitting curves.

point is expected to shift to higher frequency values, decreasing the crosstalk at a higher rate.

Apart from the thermal parameters of the substrates material, it is observed that the crystal structure of the substrate also affects the response of the bolometers. The bolometers made on $SrTiO_3$ did not show much dependence on back-etching; however back-etching the $LaAlO_3$ substrate-based bolometers considerably affected the response at an unexpectedly low modulation-frequency range.

3.5 Effect of the Substrate Back-etching

Basically, back-etching removes the interface between the substrate and the cold-head. Thus, there should be no effect of Kapitza boundary resistance. For example, the thermal diffusion length of $SrTiO_3$ based bolometers, shown in Figure 3.8, is 1 mm at 4 Hz modulation frequency. At frequencies below 4 Hz, the heat wave is expected to face the boundary resistance that reduces the phase of the response [70], [71]. However, since there is no such boundary in the back-etched bolometers, the phase of the response ends up being higher compared to the normal substrate based bolometers.

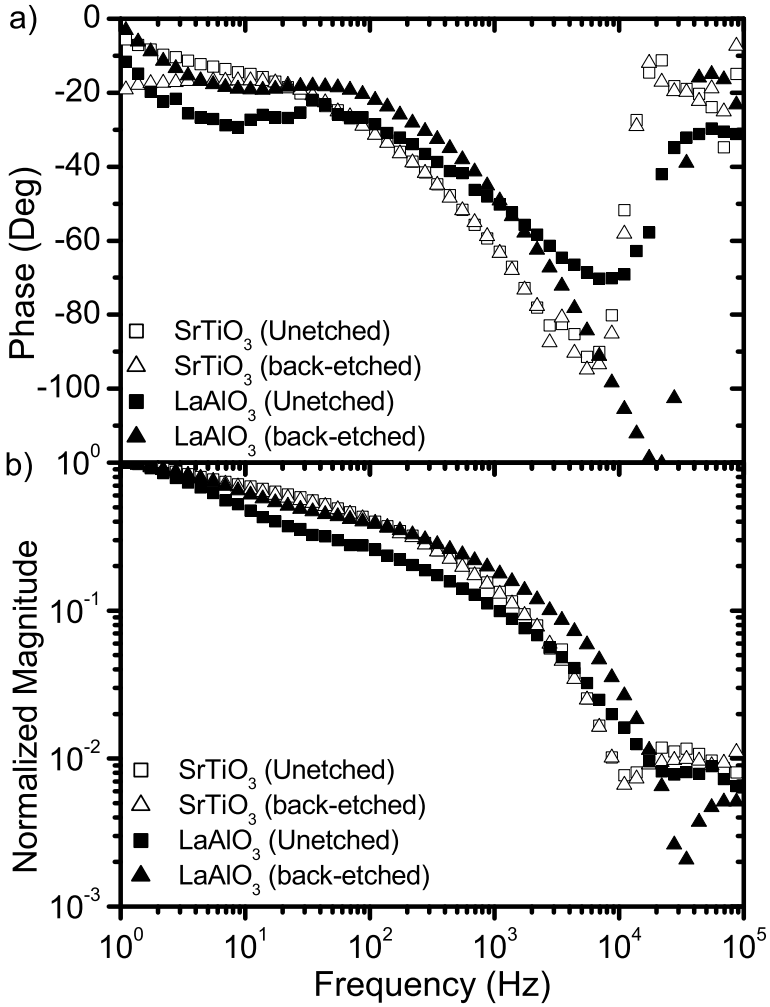

Figure 3.8: a) Phases and b) magnitudes of back-etched and unetched devices made on $LaAlO_3$ and $SrTiO_3$ substrates.

At frequencies where the propagating heat is not expected to face the boundary, the response is expected to be independent of the back-etching [24], [72]. As Figure 3.8 shows, the response of the bolometers on $SrTiO_3$ substrate was as expected. However, the bolometers made on $LaAlO_3$ showed a clear dependence on back-etching even at higher frequencies where the thermal diffusion length is supposedly much shorter than the substrate thickness. This result is different from that predicted by the classical models and needs further detailed investigation [24], [72], [73]. To verify that this was due to the substrate-specific result, we repeated the experiment with different $LaAlO_3$ and $SrTiO_3$ based bolometers; which led to similar results. Since the thermal conductance and the thermal capacitances of both substrates are close to each other, [84] we attribute this discrepancy to the twinned structure of the $LaAlO_3$ material possibly affecting the phonon propagation mechanism, the physical reasoning behind which is under investigation.

Chapter 4

Modeling the Crosstalk

In Chapter 3, we qualitatively explained the observed dependence of response behaviors on the various physical parameters of the devices. In this chapter, we propose two models to support the results of Chapter 3 and to make application specific bolometer array designs.

In this chapter we propose two models: one of them, the simple model, is basically an application of the conventional heat propagation equation to the bolometers together with the proper thermal parameters found by using the experimental data from Chapter 3. The other model, the analytical thermal model, is more robust and has two more components in addition to the principal thermal diffusion equation, the details of which is explained in Section 4.2.

4.1 Simple Model

The spatial dependence of the temperature through the substrate, for large area bolometers assuming 1D heat propagation, has been derived in Section 1.4 and formulated in [7], [72], and [73] as the following:

$$\frac{T(x,f)}{T_0} = \underbrace{\exp[-\sqrt{\frac{\pi f}{D}}x]}_{Magnitude} \underbrace{\exp[-\sqrt{\frac{\pi f}{D}}x\, j]}_{Phase} \tag{4.1}$$

Table 4.1: The crosstalk-free modulation frequencies and the calculated diffusivities for devices A, C, and D at T_{c-zero}, T_{c-mid}, and $T_{c-onset}$ for $SrTiO_3$ and $LaAlO_3$ substrates.

Substrate	Device	d	Crosstalk-free f_m (Hz)			Diffusivity (cm^2/s)*		
		(μm)	T_{c-z}	T_{c-m}	T_{c-o}	T_{c-z}	T_{c-m}	T_{c-o}
$SrTiO_3$	A	40	17853	15500	-	0.030	0.028	-
$SrTiO_3$	C	60	7590	5850	4611	0.030	0.026	0.022
$SrTiO_3$	D	170	762	645	366	0.029	0.027	0,022
$LaAlO_3$	A	40	69400	34870	-	0.109	0.086	-
$LaAlO_3$	C	60	13840	8730	-	0.086	0.073	-
$LaAlO_3$	D	170	1743	1100	-	0.104	0.095	-

* For $SrTiO_3$, average diffusivities at T_{c-zero}, T_{c-mid}, and $T_{c-onset}$ are 0.030, 0.027, and 0.022 cm^2/s respectively.
For $LaAlO_3$, average diffusivities at T_{c-zero} and T_{c-mid} are 0.099cm and 0.084 cm^2/s respectively.

Where, D is the thermal diffusivity of the substrate material, f is the modulation frequency; x is the distance from the bolometer, and T/T_o is the spatial and frequency dependent variation of the temperature in the substrate.

We have made a finite element modeling with ANSYS and observed that for a small area bolometer, the lateral thermal diffusion can be approximated with the same decay factor after a separation distance equal to the device width.

In the previously reported results, a clear knee frequency in the magnitude of the response vs. modulation frequency curve has been observed due to the Kapitza boundary resistance at the bottom of the substrate [70], [2]. However, a knee frequency is not expected in the lateral direction. Thus, we calculated the diffusivity values by using (4.1) and the response plots. For example, the phase minimum for device D, at T_c occurs at 645 Hz as obtained from Figures 3.1-a and 4.1-a and the corresponding T/T_0 value is 0.00978 as obtained from Figures 3.1-b and 4.1-b. The distance, d, between the device B and D is 170 μm. If we substitute the above values in (4.1), we get a diffusivity value of 0.027 at T_{c-mid} as shown in Table 4.2. According to [84] and [85], the corresponding diffusivity D, for bulk $SrTiO_3$ is 0.12 cm^2/s.

The diffusivity values found here which is derived from the basic thermal diffusion process differs from the previously reported values. This is interpreted to be due to the fact that our calculation here is mostly based on the lateral thermal conductance where [84] and [85] report the values for bulk material and for vertical thermal conductance. For different substrate materials, the crosstalk free modulation frequencies and the lateral diffusivity values are given in Table 4.1. From engineering point of view, one can use these lateral diffusivity values for the calculations of the lateral thermal diffusion process for design optimizations targeting crosstalk-free operation.

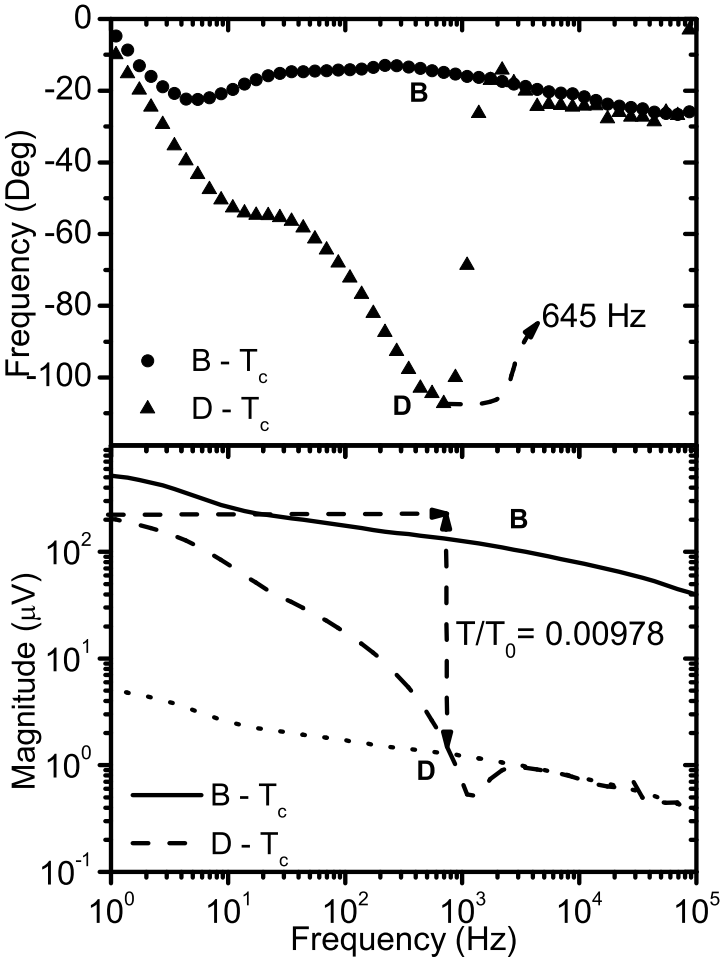

Figure 4.1: Obtaining the numeric values for the simple model from experimental data.

4.2 Analytical Model

In the previous section, we have calculated the lateral thermal diffusivity (D_L) of the $SrTiO_3$ and $LaAlO_3$ substrate materials by taking into account only the fundamental thermal diffusion equation [23], [86]. That approach is valid for quick design purposes such as deciding on the the device dimensions and the operating modulation frequency. In this section, we present a more robust model that can be also be used to explain the observed response behaviors of the characterized devices. The model has three main parts: i) effect of the lateral heat diffusion, ii) effect of the vertical heat diffusion iii) effect of the leaking input laser through the mask. These three parts are shown in Figure 4.2. Basically, the previously reported lateral thermal diffusion parameter takes into account all these three parts up to the frequency ranges that the crosstalk is not negligible. In this paper, we do not use the previously defined lateral thermal diffusivity but use the bulk thermal diffusivity of the substrate material. For comparison purposes, the results of the simple model with lateral diffusivity values is given in Section 4.2.1 as well.

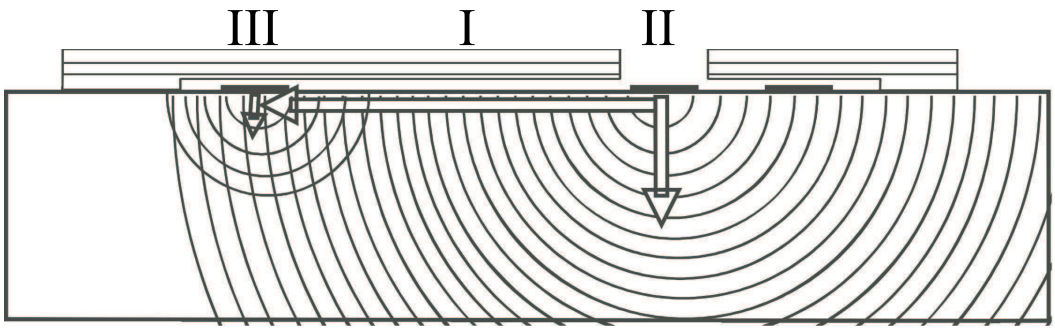

Figure 4.2: Three main parts of the analytical model: i) effect of the lateral heat diffusion, ii) effect of the vertical heat diffusion iii) effect of the leaking input laser

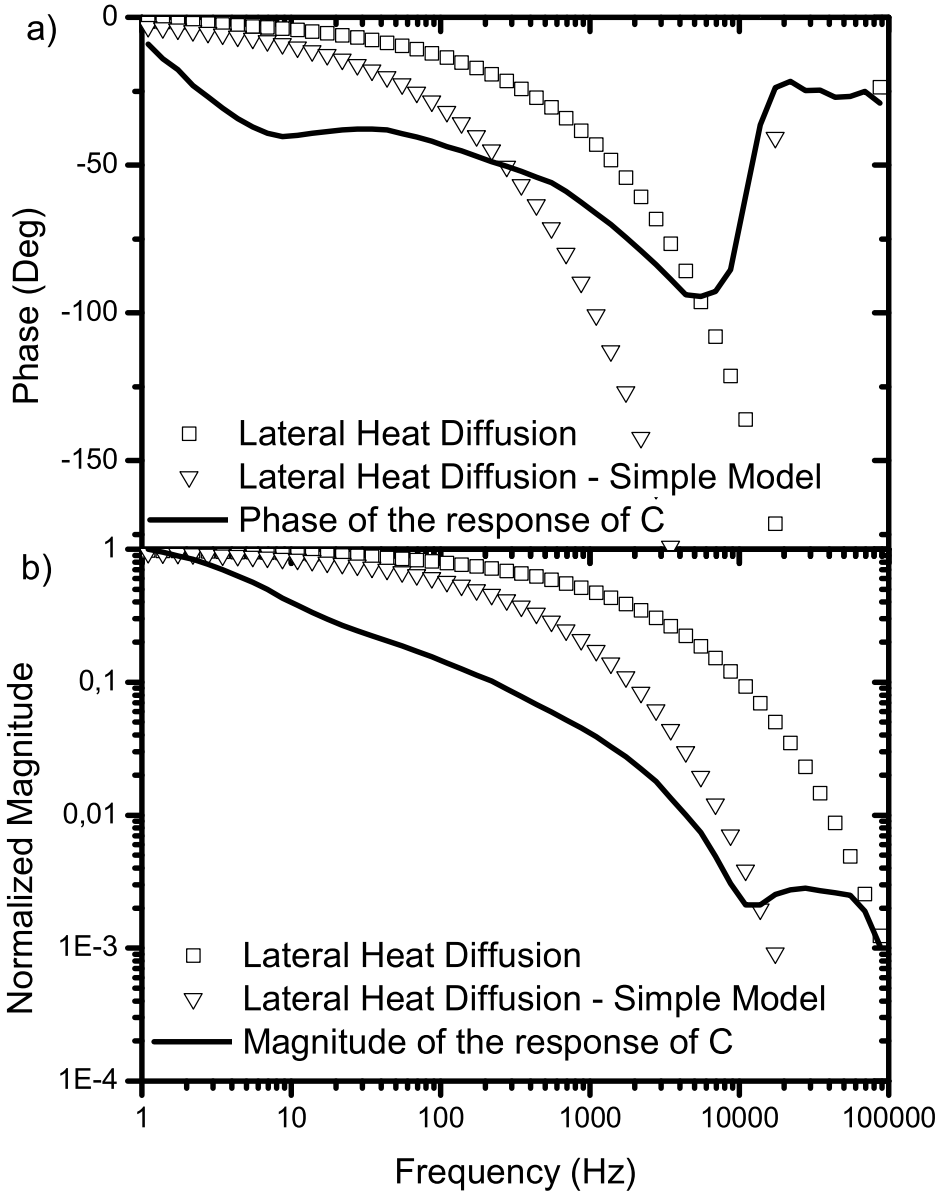

Figure 4.3: Measurement results of the response of device C (——) and thermal modeling results for lateral heat diffusion equation (□). ▽ shows results of the simple model from Section 4.1

4.2.1 Heat Diffusion on the Surface of the Substrate

Assuming only lateral heat propagation in the substrate, the spatial variation of the response at distance x away from a single pixel bolometer has been formulated as in Eq. 4.1, [7], [73].

The points represented with □ in Figure 4.3 shows the results of Equation 4.1. It is seen that the lateral heat propagation equation is not adequate for explaining the experimental data shown with straight lines in Fig 4.3. However, as in Section 4.1 for simple design purposes, a new term called lateral thermal diffusivity (D_L) was introduced and used in (4.1) [23]. The results of this approach is shown with ($\bigtriangledown$) in Fig. 4.3. As shown, it gives a better approximation than the use of bulk diffusivity of the substrate in the lateral heat diffusivity approximation.

4.2.2 Heat Diffusion in the Bulk

We have shown that for a 1 mm thick $SrTiO_3$ substrate, the substrate-cold head Kapitza boundary resistance is effective up to 4 Hz modulation frequencies [78]. In Figure 4.4, it is shown that in this array configuration there is a knee frequency around 4 Hz in the crosstalk based response as well which is due to the effect of the Kapitza resistance. Thus we cannot neglect the effects of the vertical propagation and the interfaces. However, (4.1) assumes heat propagates only in the surface of the substrate material. Hence another term has to be added to (4.1) to be able to take the thermal parameters caused by the bulk and the interfaces into account as follows:

$$r_{v-C}(f) = \underbrace{\exp[-(1+j)\sqrt{\frac{\pi f}{D}}x]}_{Lateral\,Heat\,Diffusion\,Term} \times \underbrace{(r_{v-B}(f))^{\alpha}}_{\substack{Vertical\,Heat\\ Diffusion\,term}} \tag{4.2}$$

Where, $r_{v-C}(f)$ is the measured crosstalk based response of the sense-pixel C, $r_{v-B}(f)$ is the experimental data of the device B and α is the term that accounts for amount of the the crosstalk delay caused by the substrate and the interfaces. Basically, as crosstalk lag decreases i.e. stronger crosstalk is observed, the exponential α decreases. This is an expected result since as the crosstalk between

the devices increase, the lateral heat diffusion becomes more dominant and the contribution of the deeper bulk and interfaces decrease. The result of (4.2) is shown with ◯ in Figure 4.4.

For a rough estimation of the α parameter, a relation between the lateral thermal diffusivity is found based on the D_L values given in Table 4.2 and the α values used in (4.2). As given in Table 4.2, $\alpha \times D_L$ is equal to 0.05 for $SrTiO_3$ substrate and 0.11 for $LaAlO_3$ substrate. Thus, once the lateral thermal diffusivity value of a device is known for a specific substrate, the α parameter can be estimated for the array. In Section 4.3, the utilization of the parameter α is shown with the application to devices with various physical parameters.

4.2.3 Leaking Input Laser Effect

As seen in Figure 4.4, the phase and magnitude of the crosstalk response that are shown with ◯ continuously decrease. However, after some frequency, the phase of the experimental data shown with straight line recovers and it converges to that of device B and likewise, the magnitude of device C recovers to the magnitude of B scaled by the transparency of the reflecting mask. Thus, after some frequency, the response caused by the input laser becomes dominant. The input laser leaks to the device C through the reflecting mask. If we add this leaking term to the crosstalk response, we get the following relation whose plot is shown with △ in Figure 4.4:

$$r_{v-c}(f) = \underbrace{\exp[-(1+j)\sqrt{\frac{\pi f}{D}}x]}_{Lateral\ Heat\ Diffusion\ Term} \times \underbrace{(r_{v-B}(f))^{\alpha}}_{\substack{Vertical\ Heat \\ Diffusion\ term}} + \underbrace{r_{v-B}(f) \times \beta}_{Leaking\ laser\ term} \tag{4.3}$$

In our experiments, the transparency of the reflecting mask was in the order of 1% as shown in Table 4.2. Thus at low frequencies, where the crosstalk is dominant, the effect of the leaking laser term is negligible.

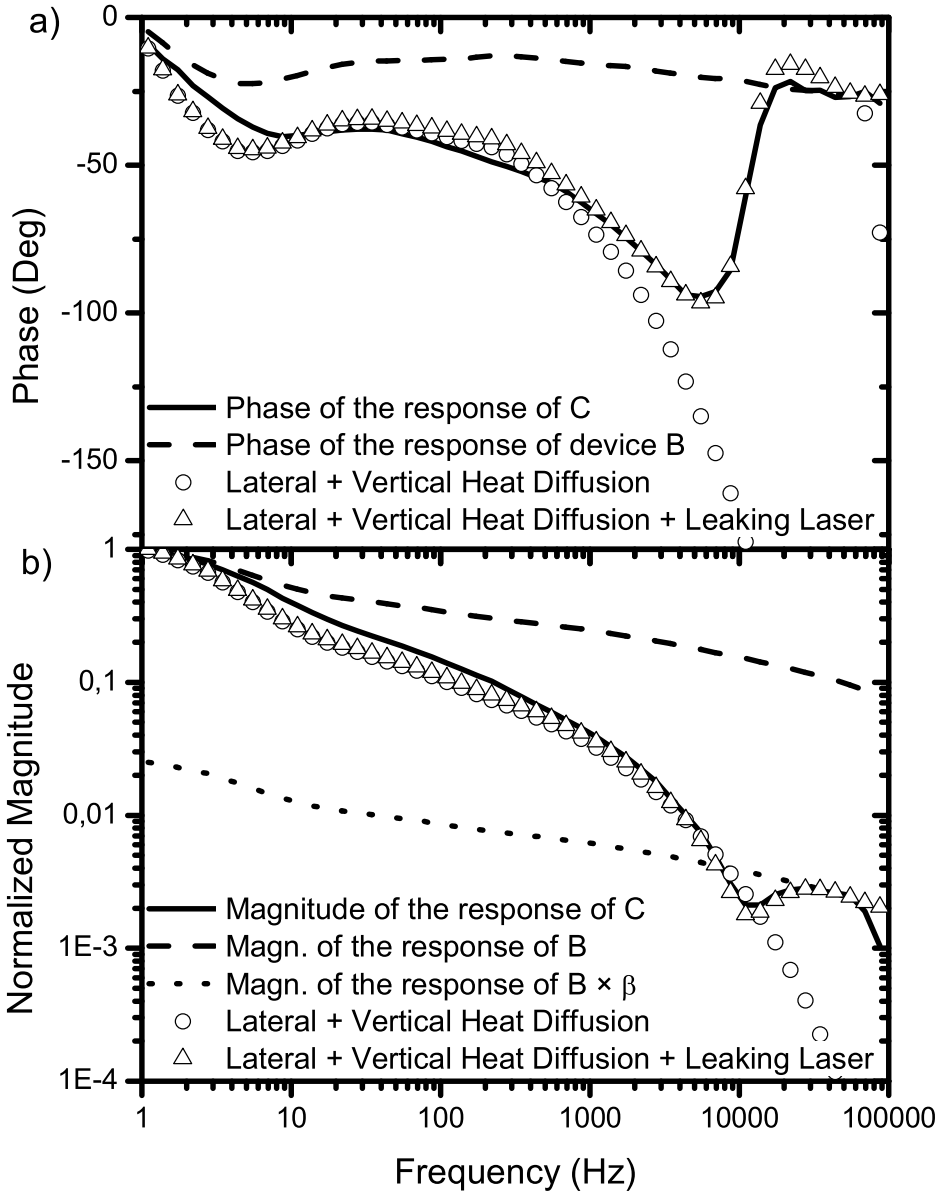

Figure 4.4: Measurement results of the response of device B (- - -) and C (——) and analytical model without (◯) and with (△) leaking laser effect. (. . .) shows the magnitude of device B multiplied by the transparency (β) of the mask.

Table 4.2: The parameters used in the application of the thermal model to the test devices.

No	Substrate	D[a] cm^2/s	D_L[b] cm^2/s	T (K)	t[c] (nm)	x[c] μm	β[c]	α	$D_L \times \alpha$
1	$SrTiO_3$	0.12	0.028	T_c	200	30	0.010	1.9	0.053
2	$SrTiO_3$	0.12	0.027	T_c	200	50	0.010	1.9	0.051
3	$SrTiO_3$	0.12	0.030	T_{c-zero}	200	150	0.010	1.75	0.052
4	$SrTiO_3$	0.12	0.026	T_c	200	150	0.010	1.9	0.049
5	$SrTiO_3$	0.12	0.022	$T_{c-onset}$	200	150	0.022	2.1	0.046
6	$SrTiO_3$	0.12	0.025	T_c	400	30	0.009	2.2	0.055
7	$SrTiO_3$	0.12	0.026	T_c	400	50	0.008	2.2	0.057
8	$SrTiO_3$	0.12	0.024	T_c	400	150	0.009	2.2	0.052
9	$LaAlO_3$	0.32	0.086	T_{c-zero}	200	50	0.015	1.3	0.11
10	$LaAlO_3$	0.32	0.078	T_c	200	50	0.009	1.5	0.11
11	$LaAlO_3$	0.32	-	$T_{c-onset}$	200	50	0.016	1.6	-

[a] $SrTiO_3$: from [84], $LaAlO_3$: 0.55 from [3], 0.28 from [78]
[b] $SrTiO_3$: from [23], $LaAlO_3$: from [86]
[c] t: Film Thickness, x: Distance from the source device, B, β: Transmittance of the mask

4.3 Application of the Model to the Test Devices

In the previous section, we have chosen an arbitrary sample's data and demonstrated the derivation and physical basis of the model. We have already explained the qualitative analysis of the effects of the physical parameters of the devices on the thermal crosstalk between the devices of an array in Section 3 and hence we will not get into the details here [23], [24]. In this section, we present the results of applying the model to devices of various physical parameters and verify its validity and test its range of applicability. We have applied the model to the 11 devices listed in Table 4.2 and obtained a fairly well fit.

In addition, once the model is tested and verified in the following subsections, we utilize the model in Chapter 5 to propose possible applications of interpixel crosstalk in the bolometer arrays.

4.3.1 Device Separation

The distance between the source and sense pixels is one of the main parameters that affect the crosstalk between the devices. As the distance between the devices starts to be comparable to the thermal diffusion length at a specific frequency, the response curves of bolometers A, C, and D start to diverge from each other as shown in Figure 4.5. Eventually, after the modulation frequency becomes high enough to cease the coupling, the devices again converge to the response of the input device, B, due to the leaking laser beam as discussed earlier.

In Figure 4.5 we see the effect of the separation, x, between the devices on the crosstalk. When we apply the model to the devices 6, 7, and 8 on the same substrate with different x values, we see that the model fits well by only varying x in (4.3). This is while other parameters are constant as listed in table 4.2.

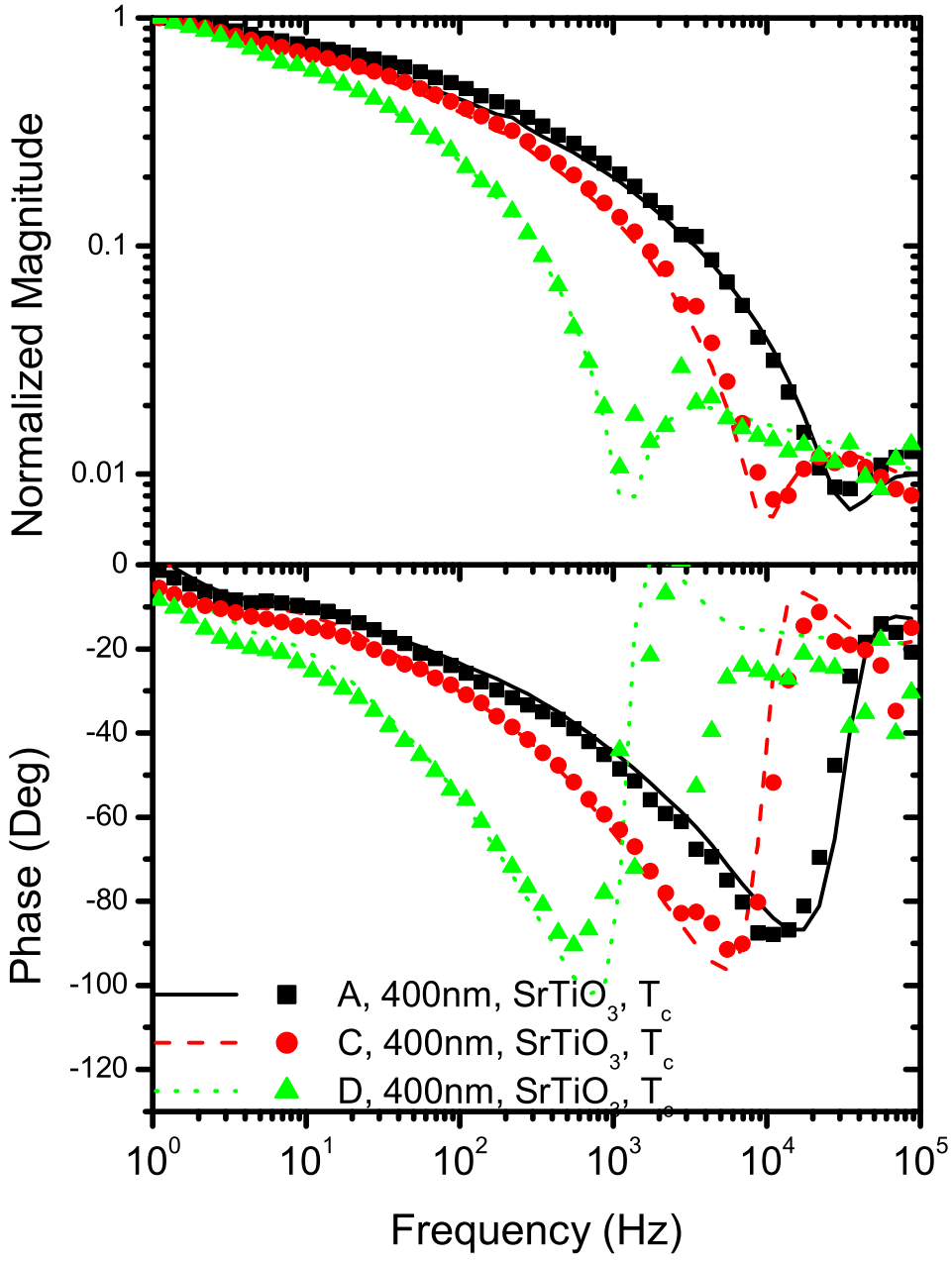

Figure 4.5: Verification of the model with the sense devices of different distances from the source device. (Table I rows 7, 8, 9) Scatter plots show the experimental date, line plots show the results of analytical model

4.3.2 Substrate Material

The thermal diffusivity of the substrate material has a major effect on the crosstalk response of the bolometers. As demonstrated in Figure 4.6, it is shown that the model is able to explain the crosstalk response for the two different kinds of substrates. As listed in the Table 4.2, the only different physical parameter between devices 2 and 10 is the diffusivity values of the substrate materials. Since the substrate has changed, the α parameter in (4.3) should be changed. $LaAlO_3$ has a lower α value than that of $SrTiO_3$. This is because the diffusivity of $LaAlO_3$ is higher leading to higher crosstalk as observed, and the thermal parameters in the vertical direction such as the interfaces are less effective on the response. In addition, the absorbtivities of the $LaAlO_3$ and $SrTiO_3$ substrates at 850 nm wavelength are 23% and 13% respectively [27]. Thus, the ratio of the absorbed radiation by the YBCO film and the substrate material is higher in $SrTiO_3$ which effects the amount of crosstalk between the devices.

4.3.3 Film Thickness

In Figure 4.7, it is shown that the model also fits very well to the crosstalk between the devices made of thicker films as well. The devices 2 and 7 are used to test the model. In this fitting, the only parameter that has changed is the α parameter. As shown in table 4.2, the thick film based device (device 7) has a relatively greater α value. We associate this to the ratio of the absorbed radiation by the film and that of the substrate material. As the film thickness is increased the amount of the absorbed radiation by the film is increased. Thus the ratio of the absorbed radiation by the YBCO film and the substrate material is higher in the thicker films. A similar variation in α parameter is observed for the substrate material effect.

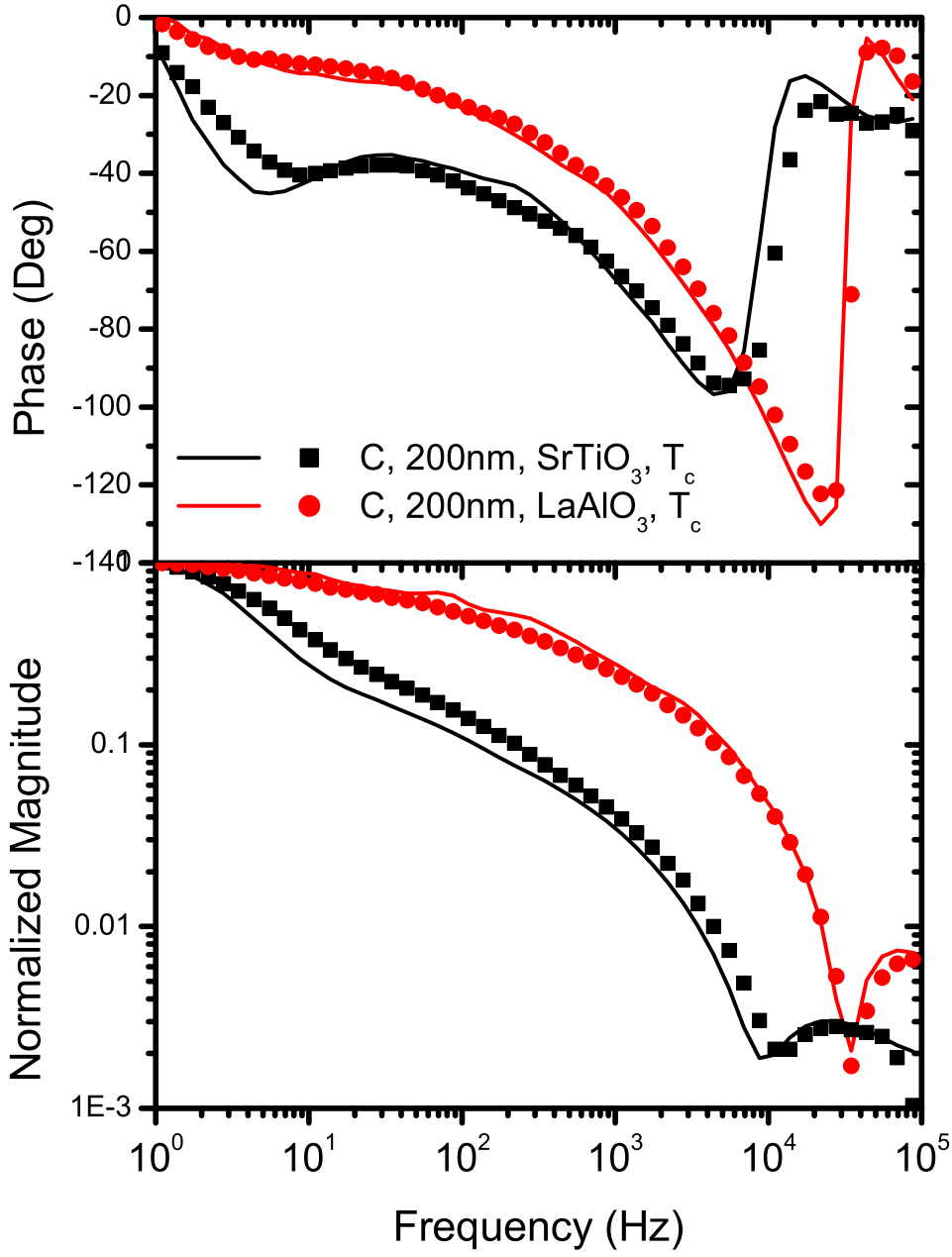

Figure 4.6: Verification of the model with the devices made on different substrate materials. (Table I rows 2, 11) Scatter plots show the experimental data, line plots show the results of analytical model.

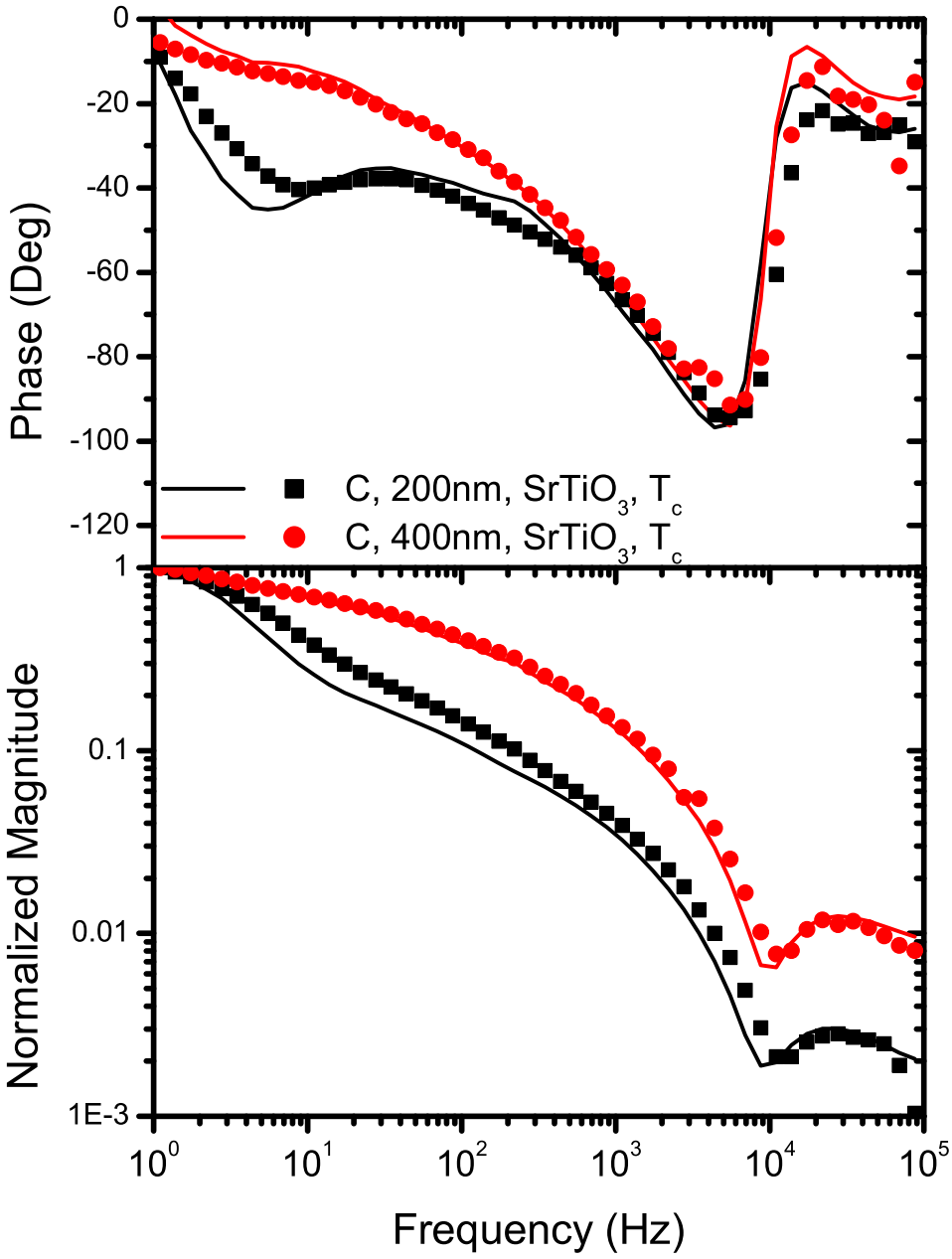

Figure 4.7: Verification of the model with the devices made of different film thicknesses. (Table I rows 2, 8) Scatter plots show the experimental date, line plots show the results of analytical model

4.3.4 Bias Temperature

In Figure 4.8, it is shown that the analytical model is able to fit the response of the devices at different temperatures. Table I shows the parameters of the devices and the parameters used in the model. We have measured the devices made on both $LaAlO_3$ (9, 10, 11) and $SrTiO_3$ (3, 4, 5) and obtained similar response behaviors. Fig 4.8 shows the experimental results and fitting curves of devices 10, 11, and 12. The temperature dependence of the crosstalk has been analyzed in Section 3.2 [23]. There, we have concluded that as the bias temperature is decreased, the crosstalk between the devices increases. Based on the observations of the Section 4.3.2, as the crosstalk is increased the α parameter is decreased, and in Table 4.2 we also see that this result is valid in the temperature effect as well.

In addition, by using the quantitative analysis and calculation of the diffusivity values based on the simple model, at different temperatures, as explained in Section 3.1, we obtained the crosstalk-free modulation frequencies and the diffusivity values given in Table 4.1. As observed from Table 4.1 the diffusivity decreases as the temperature increases. The average diffusivity values were calculated to be 0.030 cm^2/s, 0.027 cm^2/s, and 0.022 cm^2/s at T_{c-zero}, T_{c-mid}, and $T_{c-onset}$ temperatures, respectively. The increase of diffusivity as the temperature is decreased might be interpreted to be due to the change of the phonon spectrum in the YBCO film. This result agrees with the previously reported single pixel response behaviors in [71] and [70], where the phase of the response of single pixel devices are also reported to increase as the temperature decreases at high modulation frequencies due to the increase of the effective thermal conductance of the devices.

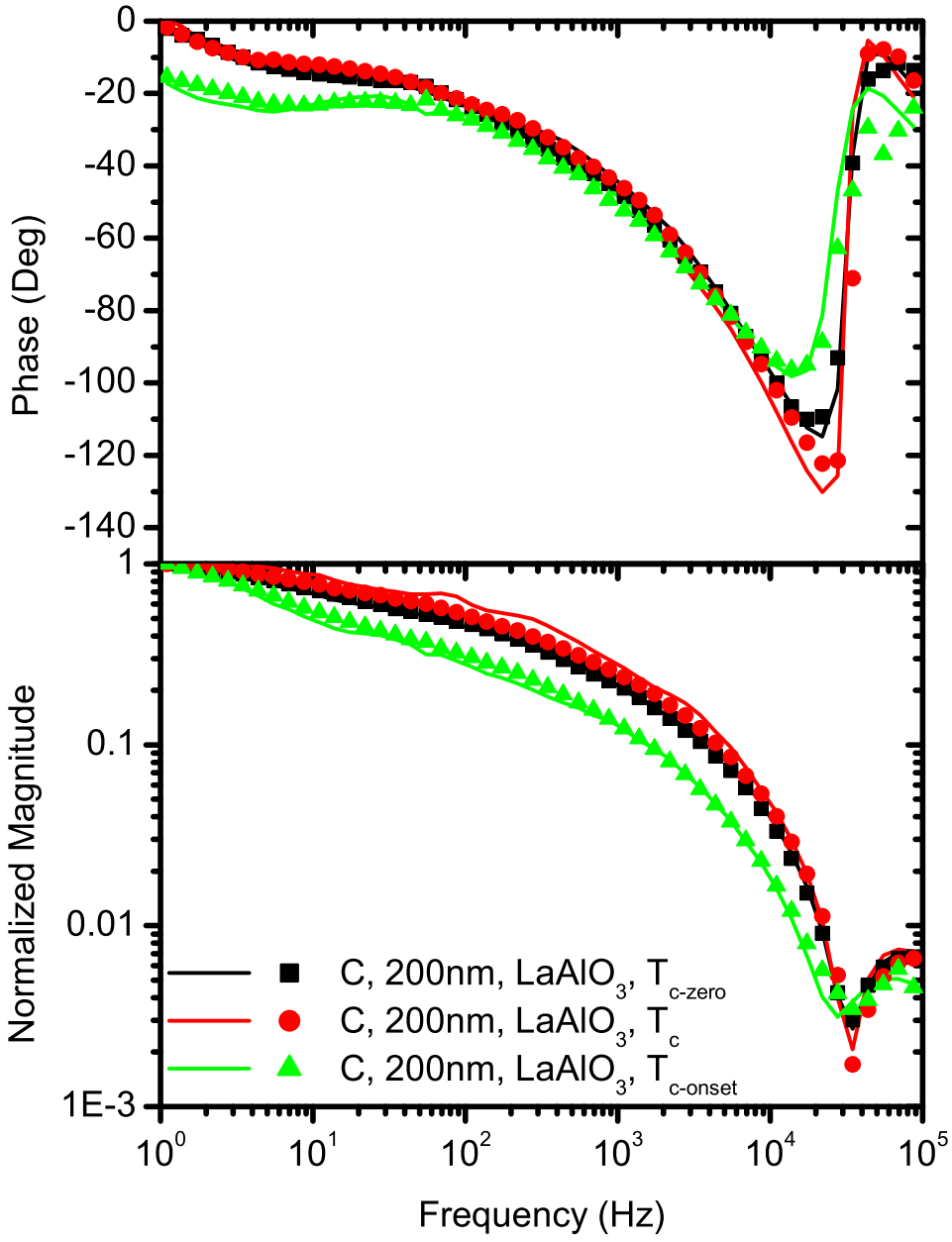

Figure 4.8: Verification of the model with the devices under different bias temperatures. (Table I rows 10, 11, 12) Scatter plots show the experimental date, line plots show the results of analytical model

Chapter 5

Applications of Crosstalk

5.1 Feasibility of Electrical-Contact Free Measurement of the Response of Superconductive Bolometer Arrays

We have investigated and reported the parameters that affect the thermal crosstalk between the neighbor pixels of the transition edge bolometer arrays and proposed an analytical model in the previous chapters [23], [86]. There, we have defined the crosstalk-free modulation frequency (f_m) for the operation of the devices operating in the conventional configuration. That is, each pixel has electrical contacts and it is favorable that the pixels do not have any thermal crosstalk.

Since a very large area on most of the detector chips is occupied by the read-out electronics and/or the contact paths, it is favorable to decrease the electrical contact areas or contacts made to the sensor pixels. Decrease of the electrical contacts when possible, would lead to denser layout designs that enables increased spatial resolution, and decrease of the power consumption as well as the fabrication costs. In this chapter, we operate the devices below their crosstalk-free modulation frequencies to utilize the crosstalk between the devices in an array in

detection of the response of the radiation sensing pixels with no electrical contacts. This is done by measuring the phase and magnitude of a read-out device in the array, which is biased using its electrical contacts. To the best of our knowledge, including semiconductor and superconductor detectors, this is the first time that such a read-out methodology is proposed and utilized. This approach would allow only one read-out pixel be used for a number of sense-pixels.

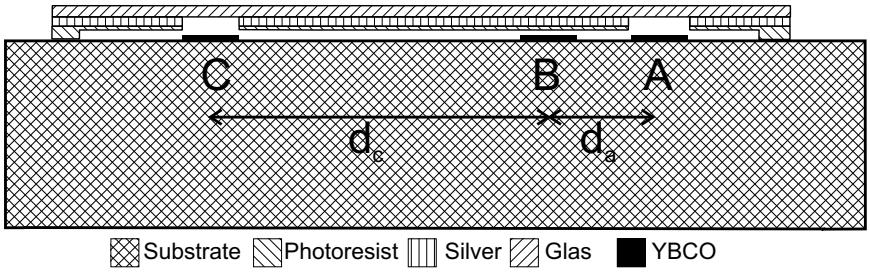

Figure 5.1: Side view of the ETB array. The read-out pixel B, and the sense-pixels A and D are shown.

In this section, we show the feasibility of the proposed read-out technique by use of two source pixels in an array, as the image-mapping devices, and one optically shielded pixel as the read-out device. While the sense pixels were electrical-contact free, the read-out device was current biased in 4-probe current-bias configuration. Both the phase and magnitude of the response due to the crosstalk in the array were found to be strongly dependent on the modulation frequency and the distance between the sense and read-out pixels. A series of measurements were designed to extract the response of each single sense-pixel. By combining the measured data, the response of individual pixels could be extracted through the interpolation of the mapped responses.

To test the feasibility of the proposed detection mechanism, we have implemented the device array configuration as shown in Figure 5.1. The read-out pixel is chosen as device B, whereas devices A and C were chosen to be the sense-pixels being exposed to the incident radiation. The device B has contacts for 4-probe measurements, and devices A and C do not have any electrical contacts. The goal of this study is to find the methodology for extracting the response of the A and C pixels through the measured signal of the current biased device B.

5.1.1 Principle of Operation

The spatial and frequency dependence of the response at distance x away from a single pixel bolometer has already been formulated in Chapter 4.

$$\frac{T(x,f)}{T_0} = \underbrace{\exp[-\sqrt{\frac{\pi f}{D}}x]}_{Magnitude}\ \underbrace{\exp[-\sqrt{\frac{\pi f}{D}}x\, j]}_{Phase} \tag{5.1}$$

Where, $T(x,f)/T_0$ is the normalized response under modulation frequency of f at x distance away from the source pixel, and D is the diffusivity of the substrate material. As shown in Equation (5.1), with the increase of the distance x, the phase of the response, $-\sqrt{\pi f/D} \times x$, decreases resulting in further increase of the lag of the signal.

Considering the crosstalk for a two-pixel case, the crosstalk response at point x_b, caused by devices A and C, are the superposition of the responses of individual pixels A and C at x_b. Equation (5.2) shows this superposition relation:

$$\begin{aligned}\frac{T(x_b,f)}{T_0} &= \exp[-\sqrt{\tfrac{\pi f}{D}}d_a]\ \exp[-j\sqrt{\tfrac{\pi f}{D}}d_a] \\ &+ \exp[-\sqrt{\tfrac{\pi f}{D}}d_c]\ \exp[-j\sqrt{\tfrac{\pi f}{D}}d_c]\end{aligned} \tag{5.2}$$

Where d_a and d_c are the distances of A and C pixels from the B pixel respectively. Figure 5.1 shows the implemented design and the structure of the array with the shadow mask. In Figure 5.2, the superposition relation is shown together with experimental data confirming the validity of the above superposition (due to the interference) assumption for $x_a = 40\,\mu m$ and $x_c = 170\,\mu m$. The read-out pixel B, will have a response due to sense-pixels A and C with x= $40\,\mu m$ and $170\,\mu m$, respectively. If we add these two responses in vector form to include both their phase and magnitude contributions, we get the curves denoted by (▲) in Figure 5.2. The three experimental curves in Figure 5.2 are obtained by three illumination configurations as; i) only A, ii) only C, iii) both A and C. The calculated

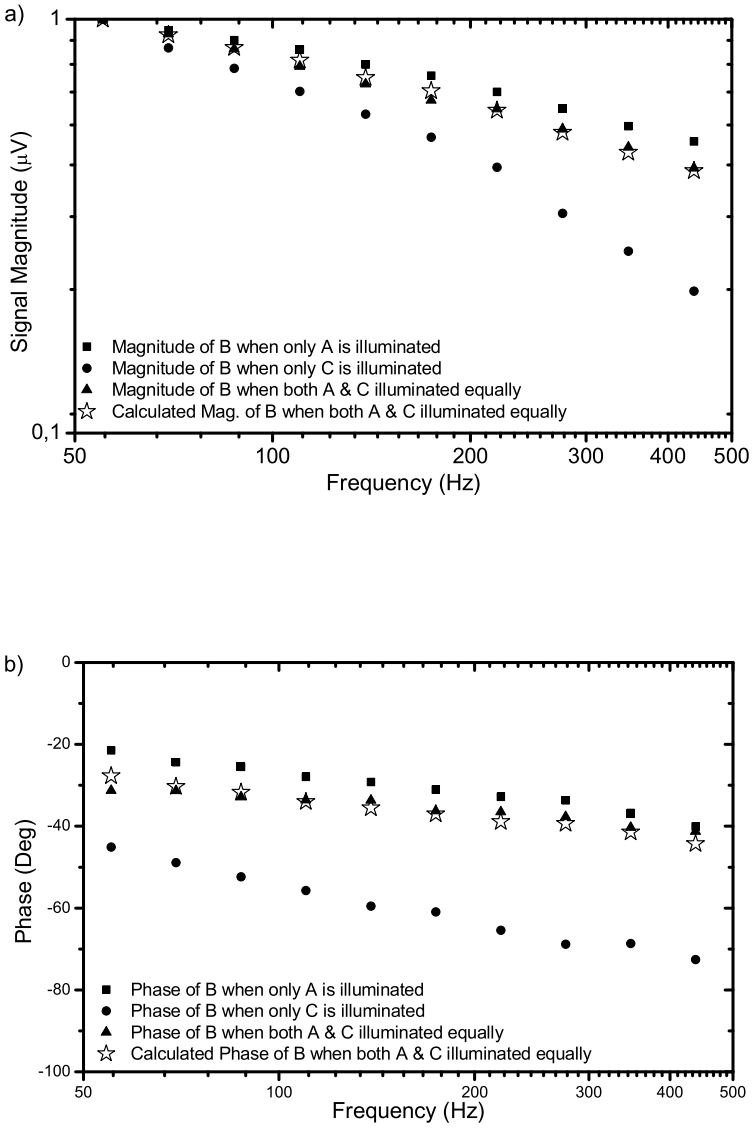

Figure 5.2: The response magnitudes (a) and phases (b) of B under various illuminations of A and C (■, ●, and ▲). The magnitude and phase of the sum of the crosstalk responses of A and C (★) fit to that of the phase and magnitude of B (▲).

curves in the Figure 5.2 are obtained by vectorial sum of individual responses of A and C. As shown in the figure, the vector sum of these responses fit closely to the case of simultaneously illumination of A and C devices, and while the phases fit well, the magnitudes do not. This is because the measurements were done at different times and due to the difficulty of the laser alignments, the magnitudes could not be perfectly aligned to the former state. However, one should note that the normalized response in the experimental curves and the calculated curve, fit very well. In the following section, we investigate the calculations in the inverse approach. That is, given the simultaneous illumination data, we extract the individual contributions of the devices A and C by using the measured phase and magnitude of superposition of the two responses.

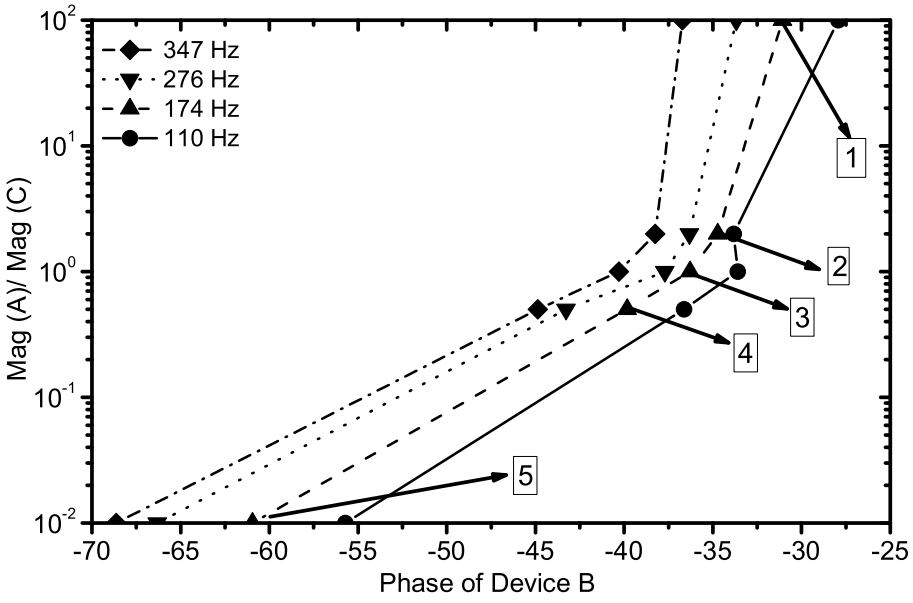

Figure 5.3: Mag(A)/Mag(C) vs. Phase of read-out device B. By measuring the phase of device B, Mag(A)/Mag(C) can be obtained. The numbers in squares show the calibration data points.

5.1.2 Example of extraction of the response of two sense-pixels with one read-out pixel

As shown in Equation (5.2), the phase of the crosstalk based response of the read-out pixel depends on the modulation frequency of the incident radiation, the distances from the sense pixels, and intensities of the incident radiation on the sense pixels. The distance between the the pixels are constant and a specific modulation frequency can be chosen. In this case, the phase of the read-out pixel is affected only by the intensities of the incident radiation on the sense pixels. Thus, by measuring the phase of the read-out pixel, the intensities of the incident radiation on the sense pixels can be obtained. To be able to achieve this, some calibration measurements are needed to be done by radiating with various intensities on the sense pixels.

For instance, at 174 Hz modulation frequency, the following calibration measurements can be done:

- When only the far sensing pixel (C) is illuminated, the phase of the read-out pixel is -61^o (taking into account the leaking laser beam, Mag(A)/Mag(C)=100),
- When the incident light on the far pixel (C) is double the near pixel (A), the phase of the read-out pixel is -40^o,
- When both of the sense pixels are illuminated equally, the phase of the read-out pixel is -36^o,
- When the incident light on the near pixel (A) is double the far pixel (C), the phase of the read-out pixel is -34^o,
- When only the near sensing pixel (A) is illuminated, the phase of the read-out pixel is -31^o (taking into account the leaking laser beam, Mag(A)/Mag(C)=0.01).

As shown, when the relative incident radiation on the near sense pixel increases, the phase of the response of the read-out pixel increases. In other words, the

lag of the crosstalk response decreases. When a proper modulation frequency is chosen, the ratios of the incident radiation on the sense pixels and the phase of the read-out pixel has a one-to-one relation as shown in Figure 5.3. The data points can be interpolated to get the ratio of the incident radiation on the sense pixels. In addition, by using the analytical model proposed in Section 4.2, or the individual pixels response data given in Chapter 3, the exact values of the responses can be obtained by using the read-out pixels data.

For example, at 174 Hz, the crosstalk response magnitude of devices A and C are 31.8 μV and 10.1 μV respectively as experimentally reported reported in Chapter 3 or predicted by the analytical model proposed in Section 4.2. Thus, when the A and C pixels are illuminated equally, the relative effect of the crosstalk of these pixels on the read-out pixel is 31.8/10.1 = 3.1 That is, the data points in Figure 5.3 should be reevaluated by taking into account this ratio, which is named as k_1.

If we formulate the crosstalk response as the superposition of the responses of A and C pixels on B pixel based on Equation (5.2):

$$V_b e^{-j\theta_b} = V_a e^{-j\theta_a} + V_c e^{-j\theta_c} \tag{5.3}$$

Where, V_a and V_c are the magnitudes of the responses of the pixels A and C, θ_a and θ_c are the phases of the responses of pixel A and C when only pixels A and C are illuminated. θ_b and V_b are the measured response phase and magnitude of the read-out pixel. Above, θ_a and θ_c values are given as -31^o and -61^o respectively and the desired unknowns are V_a and V_c in terms of V_b. A relationship between V_a and V_c can be defined as the following:

$$V_a = k_1 \times k_2 \times V_c \tag{5.4}$$

Where k_1 is the relative effect of the crosstalk of A and C pixels on the read-out pixel at a given modulation frequency and k_2 is the ratio of the radiation intensity falling on the pixels A and C as found from calibration Figure 5.3. If Equation (5.4) is substituted into Equation (5.3):

$$\frac{V_b}{V_c} = \frac{k_1 \times k_2 \times (e^{-j\theta_a}) + (e^{-j\theta_c})}{(e^{-j\theta_b})} \tag{5.5}$$

For example, to get the individual response magnitudes of A and C, given that the response of the read-out pixel is $100e^{-j35^o}$ at f_m=174 Hz, we look at the calibration Figure 5.3 for $\theta = -35^o$ and we find the value of k_2 which is 2. At 174 Hz, k_1, θ_a, and θ_c parameters are known to be constant for a specific device pattern and substrate material. If we substitute all the known values, into Equation (5.5), we get the following:

$$\frac{V_b}{V_c} = \frac{2 \times 3.1 \times (e^{-j31^o}) + (e^{-j61^o})}{(e^{-j34^o})} = 7.08 + j0.12 \cong 7.08 \tag{5.6}$$

Thus, $V_c = V_b/7.08$ and $V_a = 3.1V_b/7.08$. For $V_b = 100\mu V$, V_a and V_c values are found as 87.5 μV and 14.1 μV respectively.

By using the calibration plot of the Figure 5.3, we can obtain V_a and V_c values for arbitrary θ_b values in the range of calibration. For example for $\theta_b = -36^o$, k_2 is found to be 1 and we get $V_b/V_c = 4 - j0.15 \cong 4$ and for $\theta_b = -40^o$, k_2 is found to be 0.5 and we get $V_b/V_c = 2.5 - j0.11 \cong 2.5$. Note that V_b/V_c in Equation (5.5) is not real for arbitrary values of θ and k. However, as shown, the V_b/V_c ratio is almost real for different intensities falling on A and C pixels. This shows too that the proposed approach is correct.

Though there are a number of parameters to be taken into account in the extraction of the individual responses, one should note that all the parameters except k_2 is constant for a fixed device pattern and modulation frequency. Since only k_2 is dependent on the incident radiation, once the device dimensions and f_m are given, the individual magnitudes can be obtained by only using Equation (5.5) and calibration Figure 5.3, which give the k_2 value for a desired phase of the read-out pixel.

5.1.3 Determination of Optimum Modulation Frequency Based on the Device Dimensions

For uniquely determination of the response of A and C devices, the Mag(A)/Mag(C) vs. phase plots should have one-to-one correspondence. e. g., the curve of 110 Hz in Figure 5.3 cannot be used for this purpose. In the lower end of the frequencies, since L_f is greater than the device separations, the devices A and C are coupled to each other as well. Based on the thermal diffusion length relation $L_f = (D/\pi f)^{1/2}$ and using the thermal diffusivity of 0.027 cm^2/s, the crosstalk-free f_m between the devices A and C would be 19.4 Hz. Below this frequency, we cannot differentiate the response of device A from device C. Above the crosstalk-free f_m of device C and B, which is around 500 Hz, the response measured by the read-out pixel B would only be due to the device A. Thus we should keep the f_m above 20 Hz and below 500 Hz. The most optimum operating frequencies for this given configuration is the frequencies that are just below the crosstalk-free f_m between B and C. In Figure 5.2, we see that the optimal operating frequency is around 250 Hz where the maximum phase difference between A and C pixels is obtained, and well fits our estimation range.

5.1.4 Determination of Optimum Device Layout Dimensions Based on the Modulation Frequency

The studied bolometer array was mainly designed for investigation of the inter-pixel crosstalk of the neighbor devices, rather than the non-contact measurement of the IR response. Hence the extraction of the individual signals cannot be done efficiently for the studied devices. In this case the error margins are large and the usable range of the modulation frequencies is narrow.

As a design consideration, two main issues should be taken into account. First, the phases of the response caused by the individual sense-pixels should be as different as possible. This is while the crosstalk magnitudes of the responses should be as close to each other as possible. To be able to achieve both of

these preferences at the same time, apart from the device separations, the sizes of the sense-pixels should also be chosen different accordingly. For example, if the distant devices are made larger in area, then the magnitude of the crosstalk response on the read-out pixel would be greater. Though the phase of the response is dependent on the distance and it would not change considerably. In some applications, different sizes of sense-pixels might not be desired. In this case, the read-out pixel shape would need to be adjusted so that the desired responses from the sense-pixels are obtained. In the following section, an example design given based on these considerations and the analytical thermal model.

5.2 Design example for a read-out for 4 pixels

By using the analytical model, we propose a read out algorithm for 4-pixels. The read-out pixel is designed to be a spiral pattern and the sense pixels are put with various distances to the sense pixel as shown in Figure 5.4. The perpendicular parts of the spiral to the sense pixels are to be deposited by gold so that they do not contribute to the response.

In addition, as explained in Section 5.1.4, for maximum resolution, the phase differences between the sense pixels should be as much as possible while the magnitudes should be as close as possible. For maximum phase difference, the distances between the sense and read-out pixels can be adjusted. However, as the distance between a pair of sense and read-out pixel increases, the magnitude of the crosstalk is decreased below the measurable limit. To overcome this problem, we set the widths of the read-out pixels as a design parameter. Thus, the electrical resistances of the parallel R1-R4 portions of the read-out pixel are not the same. While designing the layout shown in 5.4, we have the freedom of changing the distances between R and S pixels and widths of R1-R4 pixels. Though the gold coated portions of the read-out pixel does not contribute to the response, their lengths affect the operating frequency range of the device. So, it can be considered as a design parameter as well.

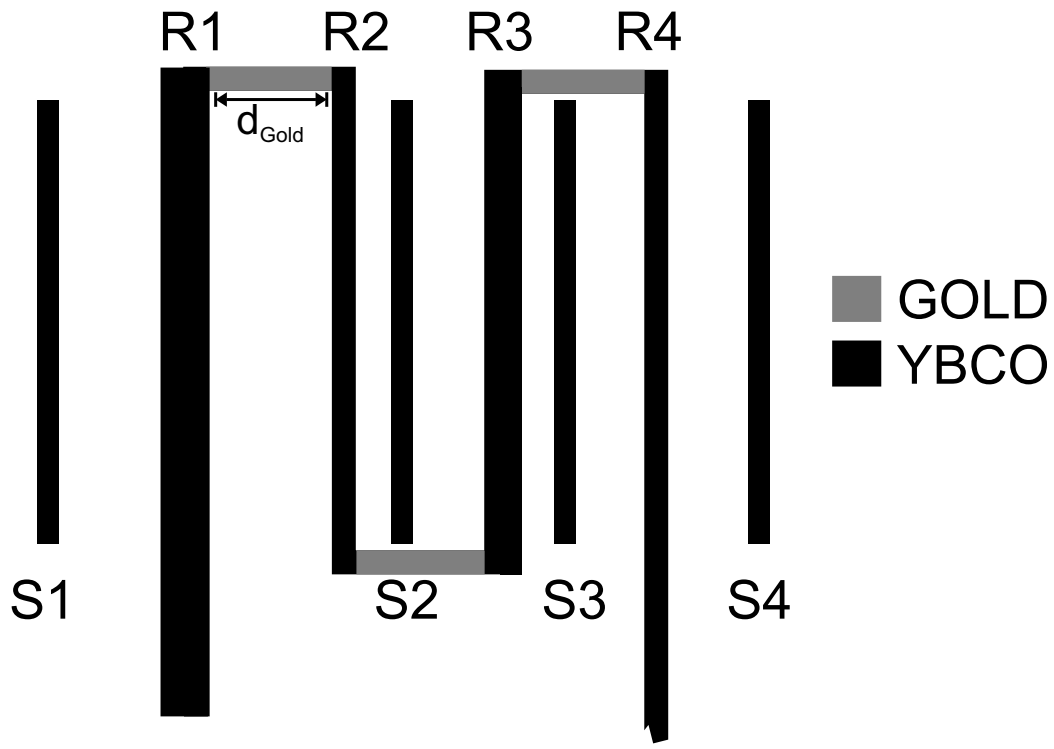

Figure 5.4: Top view of the proposed design example for a read-out for 4 pixels. Not to scale.

The overall response of the read-out pixel is a superposition of 17 components. 16 components are for the interpixel crosstalk between the sense (S) and read-out (R) pixels and 17^{th} component is for taking into account the leaking laser effect due to imperfect blocking of the reflecting mask.

If we assume that only the sense pixel S1 is illuminated, it will have an effect on the R1-R4 parts of the read-out pixel. Ignoring the leaking laser effect, we will have the following relation:

$$\begin{aligned}\frac{T_{S1}}{T_0} = R_{R1} \times e^{-(1+j)\sqrt{\frac{\omega}{2D}}d_{s1R1}} + R_{R2} \times e^{-(1+j)\sqrt{\frac{\omega}{2D}}d_{s1R2}} \\ + R_{R3} \times e^{-(1+j)\sqrt{\frac{\omega}{2D}}d_{s1R3}} + R_{R4} \times e^{-(1+j)\sqrt{\frac{\omega}{2D}}d_{s1R4}}\end{aligned} \tag{5.7}$$

Where, R_{R1} - R_{R4} are the normalized electrical resistances of the R1-R4 pixels respectively and $d_{s1R1} - d_{s1R4}$ are the distances of the sense pixel S1 to read-out pixels R1-R4.

If all of the sense pixels are illuminated, the overall response will be as the following:

$$T_S = T_{S1} + T_{S2} + T_{S3} + T_{S4} \tag{5.8}$$

Note that T_{S1} - T_{S4} will be calculated as in Equation 5.7.

In addition to the crosstalk terms caused by the sense pixels, the leaking laser term should be taken into account as well. Thus the overall response becomes as the following:

$$T = T_S + \underbrace{\beta(R_{R1} + R_{R2} + R_{R3} + R_{R4})T_{R-N}}_{Leaking\ laser\ term\ (T_R)} \tag{5.9}$$

Where β is the transparency of the reflecting mask, and T_{R-N} is the experimentally obtained normalized response of the read-out pixel. Basically, the leaking laser term, T_R, is a scaled form of the response of the read-out pixel to the IR illumination in the absence of the sense pixels.

By using Equation 5.9, we can obtain the response of the read-out pixel by any illumination combination of the sense pixels. For example, let the 2^{nd} and 3^{rd} pixels of the array are illuminated, then we get the following response according to Equations 5.7 – 5.9:

$$T = T_{S2} + T_{S3} + T_R \tag{5.10}$$

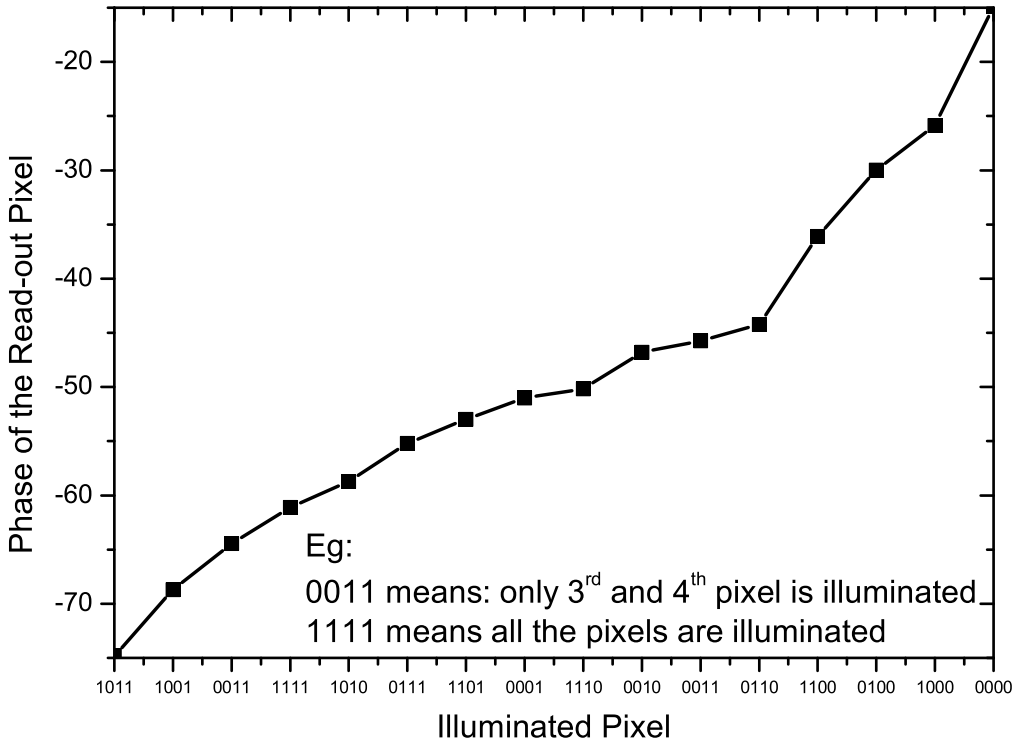

Figure 5.5: Illuminated sense pixels vs. the phase of the response of the read-out pixel

If we compute the overall response with all the 16 illumination possibilities of the sense pixels as shown in Equation 5.10, such as: 1^{st} and 2^{nd} sense pixels are illuminated (0011) or 2^{nd} and 3^{rd} pixels are illuminated (0110) or all the pixels are illuminated (1111); we get the response curve shown in Figure 5.5. The curve, has been obtained by using the physical parameters shown in Table 5.1. These parameters have been determined by automated trial and error by using Mathematica program. They might not be the optimum parameters, however, they show the feasibility of the proposed methodology.

R_{R1}	R_{R2}	R_{R3}	R_{R4}	d_{s1R1}	d_{s2R2}	d_{s3R3}	d_{s4R4}	d_{Gold}	f_m
2.5	1	1	1.5	190 μm	15 μm	50 μm	105 μm	200 μm	276 Hz

Table 5.1: Physical parameters used in computation of the thermal crosstalk by using Equation 5.8

As shown in Figure 5.5, there is a one-to-one relationship between any combination of illuminated pixels and the phase of the response of the read-out pixel. Thus, by measuring the phase of the read-out pixel, one can estimate the illuminated pixels in the array. Note that this algorithm assumes that the incident radiation power on the sense pixels are equal.

Chapter 6

Conclusions and Future Work

6.1 Conclusions

In this thesis, we investigated the dependence of the crosstalk between the pixels of bolometer arrays with various device parameters. It was found that while some device parameters cannot be freely chosen due to practical constraints, there are still enough controllable parameters for getting the desired response characteristics based on the application. In addition we have shown an analytical model for explaining the crosstalk response behaviors of the bolometer arrays.

We have shown that, as in the previously reported single pixel cases, the superconductivity transition in our bolometer arrays have a major effect on the thermal coupling between the devices and the lateral heat diffusion in the substrate. We have found that the response of the source-device shown in Figure 2.1 does not show considerable temperature dependence which is interpreted to be due to the dominant thermal conductance through the gold layer on the contact paths. Thus, the measured temperature dependent response of the devices A, C, and D are associated to be caused mainly by the superconductivity transition dependent crosstalk between the devices. This implies that the phonon scattering and its spectrum in the substrate material should also be a function of the superconductivity parameters of the thin YBCO film at the transition. This

is while the thickness of the engaged substrate material is orders of magnitude thicker than that of the YBCO film. These phenomenon is also observed at relatively high temperatures of about 90 K where the phonons' mean free paths are expected to be very short compared to the thermal diffusion length at the corresponding frequencies.

We observed that also the film thickness is one of the effective parameters that affects the crosstalk and as the film thickness is increased the crosstalk increases. We also observed that the response of $LaAlO_3$ substrate devices unexpectedly strongly depends on the back-etching even at high frequencies where the thermal diffusion length is expected to be smaller than the substrate thickness. The responsible mechanisms for this observation are under further investigation.

In addition to above investigations, an analytical model has been proposed and verified for explanation of the dependence of the crosstalk on the physical parameters of the devices, bias temperature, and the modulation frequency. We have shown that if the modulation frequency is high enough, in addition to the crosstalk based response, the leaking laser term due to imperfect blocking of the mask, should also be taken into account.

Our proposed thermal model is suitable for detailed design and implementations of edge transition bolometer arrays. It requires an experimental data from a single pixel device to be able to extend the lateral heat diffusion equation to a 3D model. At first sight, requirement of a single pixel response data may seem as a weak point of the model. But practically obtaining the response data for a single pixel device is trivial and it is not necessary to get the data for each and every single device. In this regard, the data can be tabulated for different substrate materials and film thicknesses. To make the model free of experimental single pixel device data, the single pixel bolometer model that has been explained at the Introduction chapter of the thesis can be used. We think that this only complicates the model without gaining much in terms of practical use.

Apart from the conventional device parameters, such as the device dimensions, thermal capacitance or conductances, the model introduces a new parameter, α. As discussed before in this thesis, α is a measurable parameter and it is

a measure of crosstalk amount and has a systematic dependence on the other device parameters. We observed that as the crosstalk is increased the α parameter decreases, which is verified by the substrate effect and the temperature effect. As the ratio of the absorption of the film to substrate increases the α parameter decreases, which is verified by the substrate effect and film thickness effect study. As shown, $\alpha \times D_L$ has a constant value for a specific substrate and this is inline with the above two observations.

Normally, interpixel crosstalk is an undesired issue in the array applications. However we have utilized the crosstalk phenomenon in our bolometer arrays. We have proposed and experimentally demonstrated the feasibility of a crosstalk-based read-out algorithm for transition edge bolometers. To the best of our knowledge, including semiconductor and superconductor detectors, this is the first time that such a read-out methodology is proposed and utilized. This approach would allow only one read-out pixel be used for a number of sense-pixels.

6.2 Future Work

In this thesis we investigated and modeled the thermal crosstalk in the YBCO transition edge bolometers. Now that we have a fairly good understanding of the crosstalk phenomenon and the analytical model for thermal crosstalk, the application areas of the findings can be extended.

One of the current research in the field of bolometer and SQUID applications is that to be able to read-out the response of as many pixels as possible in a bolometer array by using a single SQUID [13], [30], [32]. The proposed read-out methodology in Chapter 5 can be extended to use SQUID based read-out of bolometer arrays.

One fundamental problem in this integration is that the optimum operating temperatures of YBCO transition edge bolometers are around T_c (90K) where as the optimum and popular operating temperature of a YBCO SQUID is 77K. To

be able to integrate these two devices, preferably on-chip, the operating temperature of the bolometer should be shifted towards 77K. This is possible through Silicon ion implantation to the YBCO film. X. He *et al.* have shown that Si or Ni ion implantation can be used to shift the critical temperature of YBCO films continuously to lower temperatures and at the operating temperature the bolometer has a exactly defined temperature sensitive area which results in no change in the responsivity of the bolometer [87], [88]. In another study, one of our collaborators have reported successful Si and Ge ion implantation results to YBCO in recent years [89], [90]. Thus, the crosstalk based read-out or bolometer response by SQUID sensors is feasible and it is planned to be test in the following year.

List of Publications

1 A. Bozbey, M. Fardmanesh, J. Schubert, and M. Banzet, "Superconductivity transition dependence of the thermal crosstalk in YBCO edge transition bolometer arrays." *IEEE Trans. on Appl. Superconductivity*, vol. 16, no. 1, 2006.

2 A. Bozbey, M. Fardmanesh, J. Schubert, and M. Banzet, "Substrate and pattern dependence of the thermal crosstalk in YBCO edge transitionbolometer arrays," *Accepted for publication, IEEE Trans. on Appl. Superconductivity*, Mar 2006.

3 A. Bozbey, M. Fardmanesh, J. Schubert, and M. Banzet, "Electrical-contact free read-out of the response of superconductive bolometer arrays using the thermal crosstalk," *Applied Optics*, vol. 45, no. 28, 2006.

4 A. Bozbey, M. Fardmanesh, J. Schubert, and M. Banzet, "Analytical modeling of the interpixel thermal crosstalk in superconducting edge transition bolometer arrays," *Supercond. Sci. Technol*, vol. 19, no. 6, 2006.

5 A. Bozbey, M. Fardmanesh, I. Askerzade, M. Banzet, and J. Schubert, "Effects of the superconductivity transition on the response of YBCO edge transition bolometers," *Supercond. Sci. Technol.*, vol. 16, no. 12, pp. 1554–1558, 2003.

6 A. Bozbey, M. Fardmanesh, J. Schubert, and M. Banzet, "Feasibility of Electrical-Contact Free Measurement of the Response of Superconductive Bolometer Arrays Using the Thermal Crosstalk " *Journal of Physics: Conference Series*, July 2006.

7 B. Oktem, A. Bozbey, I. Avci, M. Tepe, D. Abukay, M.Fardmanesh. "Dependence of the response on the superconducting transition width of MgO substrate YBCO Edge Transition Bolometers" Submitted to *Physica C.*

8 A Bozbey, C. Acar, E. Ermis, M. Fardmanesh, L. Arda, J. Schubert, M. Banzet, "Investigation of the film thermal parameters of the YBCO Edge Transition Bolometers by means of IR response measurements up to 10MHz

modulation frequencies" in preparation for submission to *IEEE Trans. on Appl. Superconductivity.*

In addition to transition edge bolometer studies, research was also carried out on SQUID sensors. Later we will use the SQUID sensors for read-out of the response TEB arrays. SQUID related journal papers are as the following:

9 M. Fardmanesh, J. Schubert, R. Akram, A. Bozbey, M. Bick, M. Banzet, D. Lomparski, W. Zander, Y. Zhang and H.- J. Krause "Junction Characteristics and Magnetic Field Dependencies of Low Noise Step Edge Junction Rf-SQUIDs for Unshielded Applications," *IEEE Trans. on Appl. Superconductivity* vol. 13, no. 2, pp. 833-836, 2003.

10 A. Bozbey, I. Avci, R. Akram, M.Fardmanesh, M. Tepe, D. Abukay, "Differential DC-SQUID Magnetometer Design for Eliminating the Input Common Mode Signals", in preparation for submission to *IEEE Trans. on Appl. Superconductivity.*

11 R. Akram, T. Eker, A. Bozbey, M. Fardmanesh, J. Schubert, M. Banzet, "Effect of rf-bias frequency, rf-pumped power and fabrication process on the rf-SQUID signal characteristics", in preparation for submission to *IEEE Trans. on Appl. Superconductivity.*

Bibliography

[1] A. J. Kreisler and A. Gauge, "Recent progress in high-temperature superconductor bolometric detectors: from the mid-infrared to the 1235–1245, 2000.

[2] M. Fardmanesh, K. J. Scoles, and A. Rothwarf, "Control of the responsivity and the detectivity of superconductive edge-transition $YBa_2Cu_3O_{7-x}$ bolometers through substrate properties," *Appl. Optics*, vol. 38, no. 22, pp. 4735–4742, Aug 1999.

[3] S. V. M. Nahum and P. L. Richards, "Thermal boundary resistance of $YBa_2Cu_3O_{7-\delta}$ films," *Appl. Phys. Lett*, vol. 59, no. 16, pp. 2034–2036, Oct 1991.

[4] R. S. Prasher and P. E. Phelan, "Review of thermal boundary resistance of high-temperature superconductors." *Journ. of Supercond.*, vol. 10, pp. 473–484, 1997.

[5] K. Ivanov, A. Lima, H. Neff, G. Deep, I. Khrebtov, and A. Tkachenko, "Effects of electrothermal feedback on operation of high-tc superconducting transition edge bolometers," *Physica C*, vol. 12, no. 3, 2002.

[6] I. A. Khrebtov and A. D. Tkachenko, "High-temperature superconductor bolometers for the IR region," *Opticheski. Zhurnal*, vol. 66, pp. 79–86, 1999.

[7] B. Dwir and D. Pavuna, "A sensitive YBaCuO thin film bolometer with ultrawide wavelength response," *J. Appl. Phys*, vol. 72, no. 9, pp. 3855–3861, 1992.

[8] F. A. Hegmann and J. S. Preston, "Identification of nonbolometric photoresponse in $YBa_2Cu_3O_{7-\delta}$ thin films based on magnetic 1158–1160, Mar 1993.

[9] P. Neuzil and T. Mei, "Evaluation of thermal parameters of bolometer devices," *Appl. Phys. Lett.*, vol. 80, no. 10, 2002.

[10] J. Delerue, A. Gaugue, P. Teste, E. Caristan, G. Klisnick, M. Redon, and A. Kreisler, "YBCO mid-infrared bolometer arrays," *IEEE Trans. on Appl. Superconductivity*, vol. 13, no. 2, pp. 176–179, 2003.

[11] A. Gaugue, P. Teste, J. Delerue, A. Gensbittel, A. D. Luca, A. Kreisler, F. Voisin, G. substrate influence on inter-pixel crosstalk," *IEEE Trans. on Appl. Superconductivity*, vol. 11, pp. 766–769, 2001.

[12] T. May, V. Zakosarenko, R. Boucher, E. Kreysa, and E. G. Meyer, "Superconducting bolometer array with SQUID readout for submillimetre wavelength detection," *Supecond. Sci. Technol*, vol. 16, pp. 1430–1433, 2003.

[13] T. M. Lanting, H.-M. Cho, J. Clarke, M. A. Dobbs, W. L. Holzapfel, A. T. Lee, M. Lueker, P. L. Richards, A. D. Smith, and H. G. Spieler, "Frequency-domain SQUID multiplexing of transition-edge sensors," *IEEE Trans. on Appl. Superconductivity*, vol. 15, pp. 567–570, 2005.

[14] G. Chattopadhyay, J. Glenn, J. J. Bock, B. K. Rownd, M. Caldwell, and M. J. Griffin, "Feed horn coupled bolometer arrays for SPIRE Design, simulations, and measurements," *IEEE Trans. on Microwave Theory and Techniques*, vol. 51, pp. 2139–2146, 2003.

[15] B. Johnson, T. Ohnstein, C. Han, R. Higashi, P. Kruse, R. Wood, H. Marsh, and S. D. AND, "YBCO superconductor microbolometer arrays fabricated by silicon micromachining," *IEEE Trans. Appl. Superconductivity*, vol. 13, pp. 2856–2859, 1993.

[16] Z. Mai, X. Zhao, F. Zhou, and W. Song, "Infrared radiation detector linear arrays of high t_c superconducting thin films," *Infrared Phys. Technol.*, vol. 38, pp. 13–16, 1997.

[17] F. Voisin, G. Klisnick, Y. Hu, M. Redon, J. Delerue, A. Gaugue, and A. A. Kreisler, "A low noise cryogenic CMOS readout circuit for a 4-pixel superconducting infrared bolometer array." ESTEC, Noordwijk, The Netherlands: 4th European Workshop on Low Temperature Electronics, 2000.

[18] D. Yvon and V. Sushkov, "Low noise cryogenic electronics: Preamplifier configurations with feedback on the bolometer," *IEEE Trans on Nuclear Science*, vol. 47, no. 2, 2000.

[19] S. Nam, J. Beyer, G. Hilton, K. Irwin, C. Reintsema, and J. M. Martinis, "Electronics for arrays of transition edge sensors using digital signal processing," *IEEE Trans. on Appl. Superconductivity*, vol. 13, no. 2, pp. 618–621, 2003.

[20] D. J. Benford, J. A. Chervenak, K. D. Irwin, J. S. H. Moseley, R. A. Shafer, J. G. Staguhn, and E. Wollack, "Superconducting bolometer array architectures," *Proceedings of SPIE*, vol. 4855, pp. 148–162, 2003.

[21] D. J. Benford, G. M. Voellmer, J. A. Chervenak, K. D. Irwin, S. H. Moseley, R. A. Shafer, and J. G. Staguhn, "Design and fabrication of a 2d superconducting bolometer array for safire," *Proceedings of SPIE*, vol. 4857, pp. 125–135, 2003.

[22] J. A. Chervenak, K. D. Irwin, E. N. Grossman, J. M. Martinis, , C. D. Reintsema, and M. E. Huber, "Superconducting multiplexer for arrays of transition edge sensors," vol. 74, pp. 4043–4045, 1999.

[23] A. Bozbey, M. Fardmanesh, J. Schubert, and M. Banzet, "Superconductivity transition dependence of the thermal crosstalk in YBCO edge transition bolometer vol. 16, no. 1, 2006.

[24] ——, "Analytical modeling of the interpixel thermal crosstalk in superconducting edge transition bolometer arrays," *Supercond. Sci. Technol*, vol. 19, no. 6, 2006.

[25] ——, "Substrate and pattern dependence of the thermal crosstalk in YBCO edge transitionbolometer arrays," *Accepted for publication, IEEE Trans. on Appl. Superconductivity*, Mar 2006.

[26] ——, "Electrical-contact free read-out of the response of superconductive bolometer arrays using the thermal crosstalk," *Applied Optics*, vol. 45, no. 28, October 2006.

[27] A. Bozbey, "YBCO edge transition bolometers: effect of superconductivity transition on the phase and magnitude Bilkent University, Dept of EE, 2003.

[28] R. Akram, "HTSC superconducting edge-transtition infrared detectors; principles, fabrication, & charactarisation." Master's thesis, Bilkent University, Jan 2000.

[29] T. V. Duzer and C. W. Turner, *Principles of Superconductive Devices and Circuits*, 2nd ed. Elsevier, 1998.

[30] T. May, V. Zakosarenko, E. Kreysa, W. Esch, S. Anders, L. Fritzsch, R. Boucher, R. Stolz, J. Kunert, and H.-G. Meyer, "On-chip integrated squid readout for superconducting bolometers," *IEEE Trans. on Appl. Superconductivity*, vol. 15, no. 2, pp. 537–540, 2005.

[31] M. Tarasov, S. Gudoshnikov, A. Kalabukhov, H. Seppa, M. Kiviranta, and L. Kuzmin, "Towards a dc squid read-out for the normal metal hot-electron microbolometer," *Physica C*, vol. 368, pp. 161–165, 2002.

[32] T. M. Lanting, H.-M. Cho, J. Clarke, W. L. Holzapfel, A. T. Lee, M. Lueker, P. L. Richards, M. A. Dobbs, H. Spieler, and A. Smith, "Frequency-domain multiplexed readout of transition-edge sensor arrays with a superconducting quantum interference device," *Appl. Phys. Lett.*, vol. 86, p. 112511, 2005.

[33] M. Birkinshaw, "The sunyaev-zel'dovich effect," *Physics Reports*, vol. 310, no. 97, 1999.

[34] E. W. Kolb and M. S. Turner, *The Early Universe*. Perseus Books, 1990.

[35] I. Biswas, "Bolometer arrays for continuum imaging in the mm and sub-mm region," University of Virginia, Tech. Rep., 2005.

[36] J. Zmuidzinas and P. L. Richards, "Superconducting detectors and mixers for millimeter and submillimeter astrophysics," *Proceedings of the IEEE*, vol. 92, no. 10, 2004.

[37] D. J. Benford, T. Ames, J. Chervenak, E. Grossman, K. Irwin, S. Khan, B. Maffei, S. Moseley, F. Pajot, T. Phillips, J.-C. Renault, C. Reintsema, C. Rioux, R. Shafer, J. Staguhn, C. Vastel, and G. Voellmer, "First astronomical use of multiplexed transition edge bolometers," *AIP Conference Proceedings*, vol. 605, pp. 589–592, 2002.

[38] C. R. McCreight and B. A. Wilson, "Future infrared detector needs for space astronomy," NASA Ames Research Center, Tech. Rep., 1999.

[39] R. W. Romani, A. J. Miller, , B. Cabrera, S. W. Nam, and J. M. Martinis, "Phase-resolved crab studies with a cryogenic transition-edge sensor spectrophotometer," *The Astrophysical Journal*, vol. 563, pp. 221–228, 2001.

[40] Project web site, http://www.apex-telescope.org/.

[41] . Z. L. Yuan, B. E. Kardynal, R. M. Stevenson, A. J. Shields, C. J. Lobo, K. Cooper, N. S. Beattie, D. A. Ritchie, , and M. Pepper, *Science*, vol. 295, p. 102, 2002.

[42] A. J. Miller, S. W. Nam, , J. M. Martinis, and A. V. Sergienko, "Demonstration of a low-noise near-infrared photon counter with multiphoton discrimination," *Applied Physics Letters*, vol. 83, pp. 791–793, 2003.

[43] L. Hao, J. C. Gallop, C. Gardiner, P. Josephs-Franks, J. C. Macfarlane, S. K. H. Lam, and C. Foley, "Inductive superconducting transition-edge detector for single-photon and macro-molecule detection," *Supercond. Sci. Technol.*, vol. 16, pp. 1479–1482, 2003.

[44] L. Hao, J. C. Macfarlane, S. K. H. Lam, C. P. Foley, P. Josephs-Franks, and J. C. Gallop, "Inductive sensor based on nano-scale squids," *IEEE Trans. on Appl. Superconductivity*, vol. 15, no. 2, 2005.

[45] B. Cabrera, R. M. Clarke, P. Colling, A. J. Miller, S. Nam, , and R. W. Romani, "Detection of single infrared, optical, and ultraviolet photons using superconducting transition edge sensors," *Applied Physics Letters*, vol. 73, pp. 735–737, 1998.

[46] D. A. Wollman, S. W. Nam, D. E. Newbury, G. C. Hilton, K. D. Irwin, N. F. Bergren, S. Deiker, D. A. Rudman, , and J. M. M. AND, "Superconducting transition-edge-microcalorimeter x-ray spectrometer with 2ev energy resolution at 1.5 kev," *Nucl. Instr. Meth. A*, vol. 444, p. 145150, 2000.

[47] F. M. Finkbeiner, T. C. Chen, S. Aslam, E. Figueroa-Feliciano, R. L. Kelley, M. Li, D. B. Mott, C. K. Stahle, , and C. M. Stahle, "Fabrication of superconducting bilayer transistion edge thermometers and their application for spaceborne x-ray microcalorimetry," *IEEE Transactions on Appl. Superconductivity*, vol. 9, pp. 2940–2942, 1999.

[48] K. D. Irwin, G. C. Hilton, J. M. Martinis, S. Deiker, N. Bergren, S. Nam, D. A. Rudman, , and D. A. Wollman, "A mo-cu superconducting transition-edge microcalorimeter with 4.5 ev energy resolution at 6 kev," *Nucl. Instr. Meth. A*, vol. 444, pp. 184–187, 2000.

[49] P. Knobloch, C. Schildknecht, T. Kleine-Ostmann, M. Koch, S. Hoffmann, M. Hofmann, E. Rehberg, M. Sperling, K. Donhuijsen, G. Hein, and K. Pierz, "Medical thz imaging: an investigation of histo-pathological samples," *Phys. Med. Biol.*, vol. 47, pp. 3875–3884, 2002.

[50] P. H. Siegel, "Terahertz technology," *IEEE Transactions On Microwave Theory And Techniques,*, vol. 50, pp. 910–928, 2002.

[51] A. Fitzgerald, E. Berry, N. Zinovev, G. Walker, M. Smith, and J. Chamberlain, "An introduction to medical imaging with coherent terahertz frequency radiation." *Phys Med Biol.*, vol. 7, 2002.

[52] B. B. Hu and M. C. Nuss, "Imaging with terahertz waves," *Opt. Lett.*, vol. 20, pp. 1716–1718, 1995.

[53] S. Hunsche, M. Koch, I. Brener, and M. C. Nuss, "THz near-field imaging," *Opt. Commun.*, vol. 150, pp. 22–26, 1998.

[54] P. Y. Han, G. C. Cho, and X.-C. Zhang, "Time-domain transillumination of biological tissues with terahertz pulses," *Opt. Lett.*, vol. 25, pp. 242–244, 2002.

[55] D. D. Arnone, C. M. Ciesla, A. Corchia, S. Egusa, M. Pepper, J. M. Chamberlain, C. Bezant, and E. H. Linfield, "Application of terahertz (thz) technology to medical imaging," *Proc. SPIE*, vol. 3828, pp. 209–219, 1999.

[56] D. M. Mittleman, R. H. Jacobsen, and M. C. Nuss, "T-ray imaging," *IEEE J. Sel. Top. Quantum Electron.*, vol. 2, pp. 679–692, 1996.

[57] D. M. Mittleman, M. Gupta, R. Neelamani, R. G. Baraniuk, J. V. Rudd, and M. Koch, "Recent advances in terahertz imaging," *Appl. Phys. B*, vol. 68, pp. 1085–1094, 1999.

[58] R. M. Woodward, B. Cole, V. P. Wallace, D. D. Arnone, R. Pye, E. H. Linfield, M. Pepper, and A. G. Davis, "Terahertz imaging of in-vitro basal cell carcinoma samples," *Conf. of Lasers and Electro-Optics*, 2001.

[59] J. V. Rudd, D. Zimdars, and M. Warmuth, "Compact fiber-pigtailed terahertz imaging system," *Photonics West: Conf. on Commercial and Biomedical Applications of Ultrafast Lasers II*, 2000.

[60] S.-B. Lee, G. D. Hutchinson, D. A. Williams, D. G. Hasko, and H. Ahmed, "Superconducting nanotransistor based digital logic gates," *Nanotechnology*, no. 14, pp. 188–191, 2003.

[61] ——, "Digital logic gates using hot-phonon controlled superconducting nanotransistors," *IEEE Trans. on Appl. Superconductivity*, vol. 13, no. 2, 2003.

[62] D. du Boulay, "Structure, vibration and electron density in neodymium-iron-boride and some rare-earth perovskite oxides," Ph.D. dissertation, The University of Western Australia, Feb 1996.

[63] Substrate manufactuters web site, http://www.coatingandcrystal.com.

[64] Substrate manufactuters web site, http://www.mticrystal.com/supercon.html.

[65] G. Koren and E. Polturak, "Is $LaAlO_3$ a viable substrate for the deposition of high quality thin films of *Supercond. Sci. Technol.*, vol. 15, pp. 1335–1339, Aug 2002.

[66] W.-B. Lor and H.-S. Chu, "Hyperbolic heat conduction in thin-film high Tc superconductors with interface thermal resistance," *Cryogenics*, vol. 39, pp. 739–750, 1999.

[67] ——, "Efect of interface thermal resistance on heat transfer in a composite medium using the thermal wave model," *International Journal of Heat and Mass Transfer*, pp. 653–663, 2000.

[68] Z.-M. Tan and W.-J. Yang, "Propagation of thermal waves in transient heat conduction in a thin film," *Journal of The Franklin Institute*, vol. 336B, p. 074.086, 1999.

[69] L. Wang, "Solution structure of hyperbolic heat-conduction equation," *International Journal of Heat and Mass Transfer*, vol. 43, pp. 365–373, 2000.

[70] A. Bozbey, M. Fardmanesh, I. Askerzade, M. Banzet, and J. Schubert, "Effects of the superconductivity transition on the response of YBCO edge transition bolometers," *Supercond. Sci. Technol.*, vol. 16, no. 12, pp. 1554–1558, 2003.

[71] M. Fardmanesh and I. N. Askerzade, "Temperature dependence of the phase of the response of YBCO edge-transition bolometers: effects of superconductivity transition and thermal parameters." *Supercond. Sci. Technol*, no. 16, pp. 28–32, 2003.

[72] M. Fardmanesh, *High Temperature Superconductivity 2: Engineering Applications*, A. Narlikar, Ed. Springer-Verlag, 2004, pp 482-485.

[73] Q. Hu and P. L. Richards, "Design analysis of a high T_c superconducting microbolometer." *Appl. Phys. Lett.*, vol. 55, no. 23, pp. 2444–2446, Dec 1989.

[74] G. Silcox, Heat Transfer Lecture Notes, Spring 2005, www.che.utah.edu/ geoff/grad_heat/lectures/6453_les01.pdf.

[75] H. S. Carslaw, *Conduction of heat in solids.* Oxford University Press, 1986.

[76] Y. Gao and D. F. Wong, "Shaping a VLSI wire to minimize delay using transmission line model." in *Proceedings*, International Conference on Computer-Aided Design (ICCAD). San Jose, California, USA: ACM and IEEE Computer Society, Nov 1998, pp. 611–616.

[77] L. O. Chua, C. A. Desoer, and E. S. Kuh, *Linear and nonlinear circuits.* McGraw-Hill Book Co., 1987, p. 756.

[78] M. Fardmanesh, "Analytic thermal modeling for DC-to-midrange modulation frequency responses of thin-film high-T_c edge-transtition bolometers." *Applied Optics*, vol. 40, no. 7, pp. 1080–1088, Mar 2001.

[79] W. Kiyokata and S. Hayakawa, *Handbook of sputter deposition technology: principles, technology, and applications.* Noyes Publications, 1992.

[80] D. B. Chrisey and G. K. Hubler, Eds., *Pulsed laser deposition of thin films.* J. Wiley, 1994.

[81] K. K. Schuegraf, Ed., *Handbook of thin-film deposition process and applications.* Noyes Publications, 1988.

[82] C. Acar and E. Ermis, "Designing and implementing amplifier switch circuit to measure high frequency response characteristics of YBCO edge transition bolometers," Senior Design Project, Bilkent University, Dept. of EE, 2006.

[83] B. Oktem, A. Bozbey, I. Avci, M. Tepe, D. Abukay, and M.Fardmanesh, "Dependence of the response on the superconducting transition width of MgO substrate YBCO edge 0.4emNoordwijkerhout-Netherlands: International Superconducting Electronics Conference (ISEC'05), 2005.

[84] U. P. Oppenheim, M. Katz, G. Koren, E. Polturak, and M. R. Fishman, "High temperature superconducting bolometer," *Physica C*, vol. 178, pp. 26–28, 1991.

[85] M. Fardmanesh, A. Rothwarf, and K. J. Scoles, "Low and midrange modulation frequency response for YBCO infrared detectors: Interface effects on the vol. 8, no. 1, Mar 1995.

[86] A. Bozbey, M. Fardmanesh, J. Schubert, and M. Banzet, "YBCO kenar gecis bolometre dizilerinde termal baglasimin speriletkenlik gecisi ve aygit parametrelerine bagimliligi." Bolu, Turkey: III. Ulusal Yuksek Sicaklik Superiletkenler Sempozyumu, 2005.

[87] X. He, J. Musolf, E. Waffenschmidt, K. Heime, H. Wolf, and K. Pien, "Silicon Ion Implantation of YBaCuO Films for Bolometer Application," *IEEE Trans. on Appl. Superconductivity*, vol. 5, no. 2, 1995.

[88] S. H. Hongy, J. D. Banieckiy, Q. Y. May, J. R. LaGraffz, J. M. Murduckz, and H. Chanz, "Control of YBCO sheet resistance with Ni implantation," *Supercond. Sci. Technol.*, vol. 11, pp. 375–377, 1998.

[89] I. Avci, M. Tepe, U. Serincan, B. Oktem, R. Turan, and D. Abukay, "Electrical and magnetic properties of Si ion implanted YBaCuO thin films and microbridges," *Thin Solid Films*, vol. 466, pp. 37–40, 2004.

[90] I. Avci, M. Tepe, B. Oktem, U. Serincan, R. Turan, and D. Abukay, "Developing a trilayer processing technique for superconducting YBaCuO thin films by using Ge ion implantation," *Supercond. Sci. Technol.*, vol. 18, pp. 477–481, 2005.